MSc Thesis

A free-slip "speed-modulator"

Abhirath Anand

Experimental investigation of influence
of an air cavity on a turbulent boundary layer
using PIV
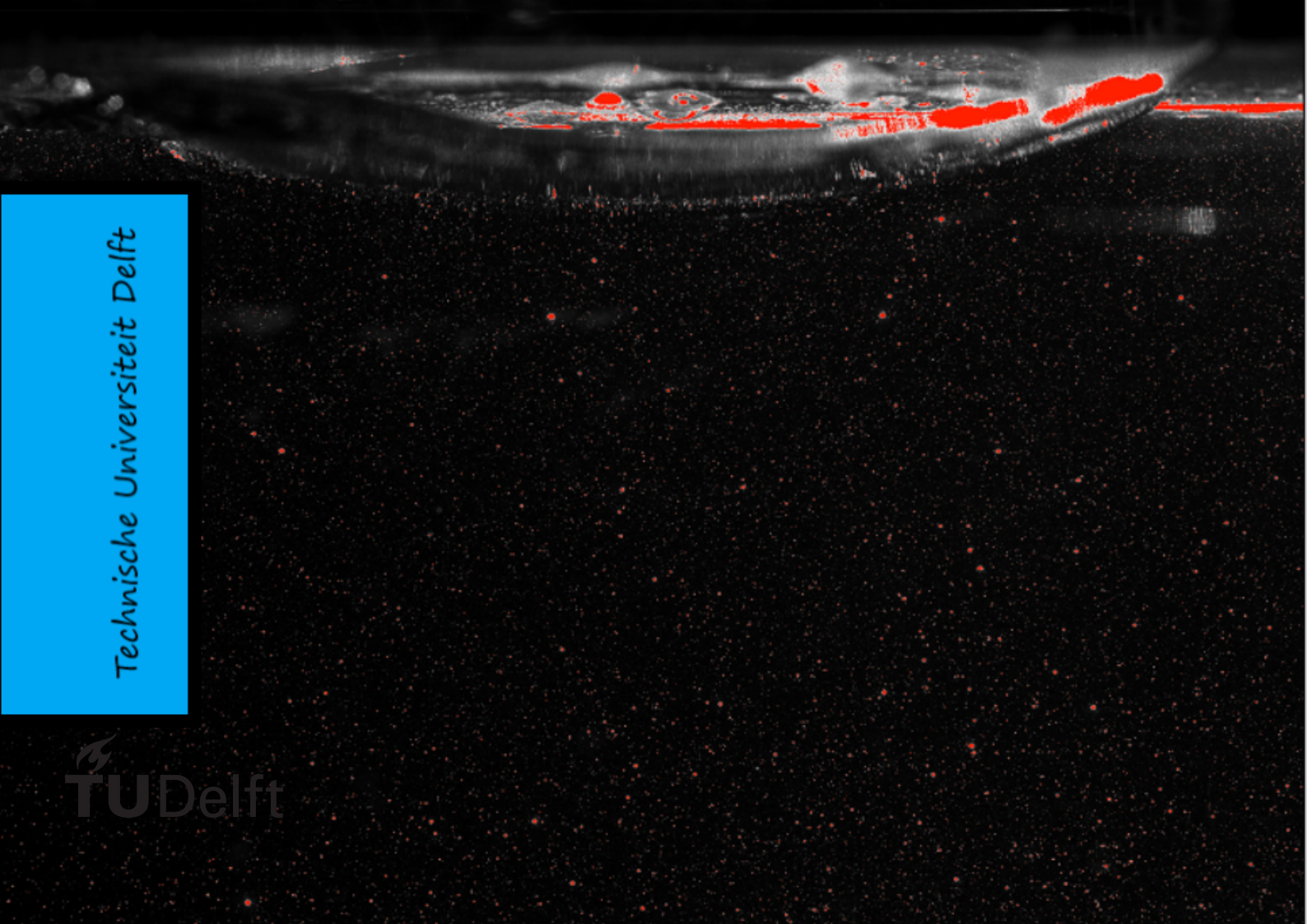
Technische Universiteit Delft

TUDelft

MSc Thesis
A free-slip "speed-modulator"

by

Abhirath Anand

to obtain the degree of Master of Science
at the Delft University of Technology,
to be defended publicly on Monday, September 27th, 2021 at 14:00 hrs.

Student number: 5081327
Project duration: November 27th, 2020 – September 27th, 2021
Thesis committee: Prof. dr. ir. Christian Poelma,   TU Delft, supervisor and chair
                    Dr. Angeliki Laskari,   TU Delft, supervisor
                    Dr. Woutijn Baars,   TU Delft
                    Ir. Lina Nikolaidou,   TU Delft

This thesis is confidential and cannot be made public until September 27th, 2021.

An electronic version of this thesis is available at http://repository.tudelft.nl/.

TUDelft

"On the scale of worlds-to say nothing of stars or galaxies-humans are inconsequential, a thin film of life on an obscure and solitary lump of rock and metal"

- Carl Sagan

Acknowledgements

Abstract

The turbulent boundary layer development under the influence of an air cavity is studied experimentally using planar PIV, with the aim of gaining insight and building upon the flow physics typically encountered in the application of air layer drag reduction. A detection technique based on correlation values is implemented to obtain an approximate shape of the air cavity and the location of the air-water interface. The technique was successful in identifying the maximum cavity thickness with sufficient accuracy. The leading and trailing edges of the cavity however, were harder to identify, the former owing to a limitation of the developed technique and the latter due to the dynamic nature of the flow and a slightly limited FOV. The ratio of the initial boundary layer thickness to the maximum thickness of the air cavity is 6.7, and as a consequence the boundary layer did not separate at the leeward side of the air cavity. The turbulent boundary layer is observed to feel the presence of the air cavity up to $8.5 - 9.5\ cm$ upstream due to an adverse pressure gradient. Alternating streamwise pressure gradients are generated due to the curvature of the air cavity: from an adverse to favourable and back to adverse. Compared to solid bump studies in literature, additional perturbations due to a free-slip boundary condition and the unstable nature of air cavity increase the complexity of the current flow. The mean velocity profile and stresses are able to capture the effects of alternating streamwise pressure gradients and air injection, with variations mostly restricted to the inner region. Effects of streamline curvature in the outer region are found to be minimal, while potential effects of the free-slip condition were much harder to identify separately and further research would be needed to appropriately assess them. The mean velocity profile is found to deviate from the classic logarithmic behaviour at the apex of the air cavity, although the flow does not seem to relaminarise. Quadrant analysis shows differences in Reynolds stress producing events compared to the baseline turbulent boundary layer case hinting at possible alteration to coherent structuring of the turbulent boundary layer developing below the air cavity.

Keywords: turbulent boundary layer; air cavity; pressure gradients; perturbations;

Contents

Nomenclature

Acronyms

SHS   Super-hydrophobic surface

BDR   Bubble Drag reduction

ALDR Air layer drag reduction

TBL   Turbulent boundary layer

PIV   Particle image velocimetry

PLIF   Planar laser induced fluorescence

HWA   Hot wire anemometry

LDA   Laser Doppler Anemometry

DNS   Direct numerical simulation

ZPGTBL Zero pressure gradient turbulent boundary layer

TKE   Turbulent kinetic energy

RSS   Reynolds shear stress

RMS   Root mean square

TI   Turbulence intensity

VLSMs Very large scale motions

CRVP Counter rotating vortex pairs

UMZ   Uniform momentum zones

Re Reynolds number

Fr Froude number

We Weber number

Flow Parameters

x Streamwise direction

y Wall-normal direction

z Spanwise direction

V   Velocity vector

u Instantaneous streamwise velocity component

v Instantaneous wall-normal velocity component

w Instantaneous spanwise velocity component

$\overline{u}$ Mean streamwise velocity component

$\overline{v}$ Mean wall-normal velocity component

$\overline{w}$ Mean spanwise velocity component

u' Fluctuating streamwise velocity component

v' Fluctuating wall-normal velocity component

w' Fluctuating spanwise velocity component

u_∞ Free-stream velocity

u_τ Wall-friction velocity

ω_z Instantaneous spanwise vorticity component

ω_z' Vorticity fluctuations of spanwise component

$\overline{\omega_z}$ Mean vorticity of spanwise component

$\overline{c}$ Mean air cavity length or Mean chord length

$t_{max,air}$ Maximum thickness of mean air cavity

$t_{max,i}$ Instantaneous maximum thickness of air cavity

τ_w Wall shear stress

δ Boundary layer thickness

δ^* Displacement thickness

θ Momentum thickness

H Shape factor $(\frac{\delta^*}{\theta})$

μ Dynamic viscosity

ρ Mass density

ν Kinematic viscosity

κ von Karman constant

Re_x Streamwise Reynolds number $(\frac{u_\infty x}{\nu})$

Re_θ Momentum thickness Reynolds number $(\frac{u_\infty \theta}{\nu})$

Re_τ Friction Reynolds number $(\frac{u_\tau \delta}{\nu})$

List of Figures

1

Introduction

Climate change is on all of our minds with a shift towards sustainable practices at the forefront of current research trends. A study by the International Maritime Organisation (IMO) has shown that green house gas emissions (GHG) due to maritime transport have increased from 977 million tonnes in 2012 to about 1076 million tonnes in 2018, a roughly 9.6% increase (Psaraftis et al. (2020)). Improving hydrodynamic performance of ships ensures a reduction in fuel consumption and hence reduced atmospheric emissions, which is closely associated with the goals of drag reduction. Skin friction drag which can be described as the drag exerted on the body as a result of the fluid present near its surface, accounts for about $60 - 70\%$ of the total drag for $\mathrm{Fr} < 0.2$ (see figure **1.1**).
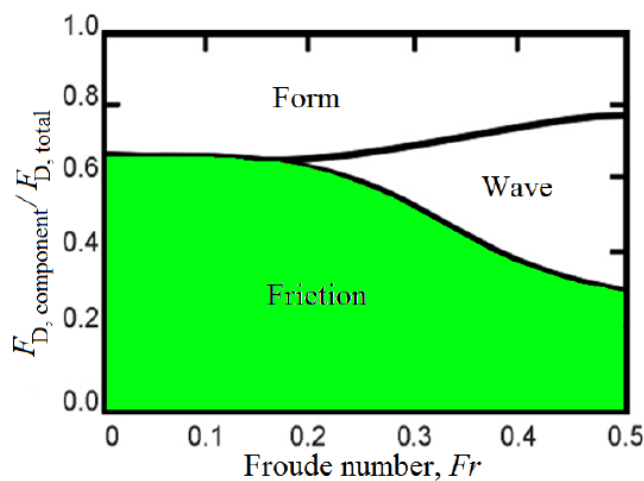
Figure 1.1: Contribution of different components of drag as a function of the Froude number(Ceccio et al. (2012))

Many drag reduction methods have been researched till date, and are generally classified into active and passive depending on whether any external source of energy is required. Passive drag reduction methods which do not require any external source of energy generally involve using polymers (Bonn et al. (2005)), bio-inspired riblets (Dean et al. (2010)), super-hydrophobic surfaces (SHS) (Fukuda et al. (2000)) or some kind of hull form optimisations. Whereas, active drag reduction methods require an external energy source for example during gas injection. Techniques such as Bubble drag reduction (BDR) (Sanders et al. (2006); Murai (2014)), Transitional Air layer Drag reduction (Elbing et al. (2008)),

Air layer drag reduction (ALDR) (Latorre (1997); Elbing et al. (2013)) fall under the active drag reduction regime (see figure **1.2**).
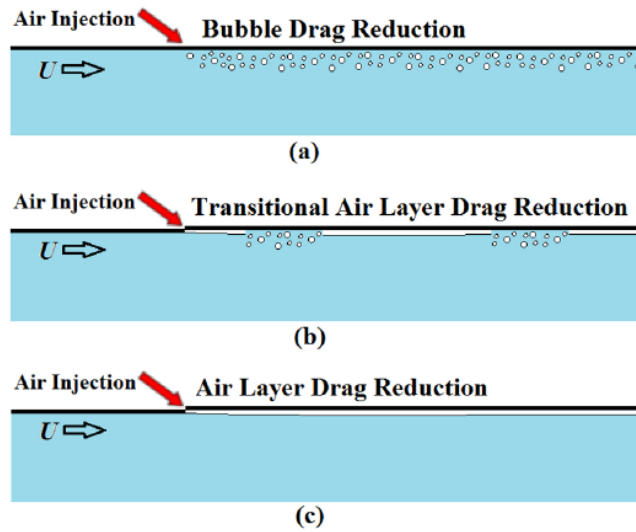
Figure 1.2: Different active drag reduction techniques (Mäkiharju et al. (2012))

At a critical gas flow rate, the bubbles coalesce to form an air layer below the hull which has a larger persistence downstream, and thus is said to contribute to more than 80% reduction in drag. The skin friction drag is curtailed due to a reduction in the wetted surface area along with a reduction in the near-wall density. This mechanism of drag reduction might not sound so simple as it is expected that the air layer modifies the momentum exchange induced by turbulence beneath the hull. The economic viability favours the ALDR showing net energy savings, and thus is currently a widely researched topic (Ceccio et al. (2010); Mäkiharju et al. (2012)). An important aspect to be addressed is the stability of the air layer as it is shown to be prone to interfacial instabilities (Kim et al. (2010)). Likewise, the turbulent boundary layer (TBL) below the air-water interface is also expected to have an effect on the interface and vice-versa. This dynamic interdependence has not been touched upon in recent literature and is the focus of this thesis.

From a fundamental perspective, studies in literature have explored TBLs subjected to different individual perturbations such as application of pressure gradients, curvature and wall roughness (Smits (1985)). The similarity with the ALDR technique lies in the fact that the air layer acts like an "obstruction" to the developing TBL, as well as creates a local change in boundary condition from a no-slip to a free-slip condition, which is likely to perturb the surrounding flow. TBLs subjected to multiple perturbations in tandem although encountered in many engineering applications (and the current one), is something that is not yet widely explored. Thus, this forms a motivation to study the development of a TBL under the influence of an air layer, which will be pursued in this thesis using the experimental technique of planar Particle Image Velocimetry (PIV).

Chapter **2** provides a theoretical background on a zero pressure gradient turbulent boundary layer (ZPGTBL) followed by a review of current studies pertaining to the application of ALDR; the scope of the current study along with the research questions are then presented. Chapter **3** provides details of the experimental technique used, the experimental parameters and data processing. Chapter **4** presents the results followed by a discussion. Finally, chapter **5** gives conclusions from this study and recommendations to improve the current research and interesting areas for future work.

2

Theoretical background and Literature review

The current chapter aims to recapitulate the theoretical knowledge of a BL and give an overview of the current literature pertaining to the problem. The basics of a BL are covered with more emphasis on different regions and scalings in a TBL, along with current interpretation of the coherent motions in a TBL. The discussion related to coherent structures will be considered only for the simplified case of a zero-pressure gradient TBL (ZPGTBL), since this thesis is also concerned with the development of a ZPGTBL.

Literature related to the active method of drag reduction, the ALDR technique is discussed with a review on various parameters relevant to this research problem. This is followed by a brief discussion on the problem's relevance from a fundamental perspective. To conclude this chapter, the literature study is summarised to get the "big-picture", and finally the research questions to be tackled, are formulated.

A right-hand coordinate system will be used with x, y and z representing the streamwise, wall-normal and spanwise directions respectively, with the corresponding components of the instantaneous velocity vector $\mathbf{V}$ being u, v and w. The mean velocities will be represented by $\overline{u}, \overline{v}$ and $\overline{w}$, and the fluctuations by u', v' and w'.

2.1. ZPGBL basics

The basics of a canonical TBL and its structuring are recaptured in this section to provide a base for this thesis.

2.1.1. Boundary layers

Boundary layers (BL) can be defined as thin regions near the wall where viscous forces and rotationality cannot be neglected, separating it from an inviscid region away from the influence of the wall which can be considered irrotational. As a uniform free stream flow encounters a flat plate, a BL tends to grow along x with its vertical extent typically characterised as δ, which can be defined as the distance away from the wall at which the velocity is $0.99u_\infty$, where u_∞ is the free-stream velocity (see Figure **2.1**).
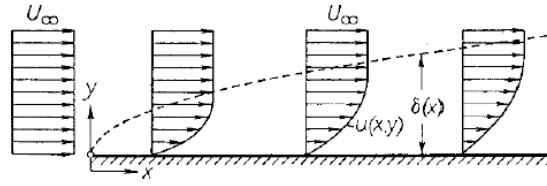
Figure 2.1: BL development over a flat plate (from Schlichting et al. (2017))

Other parameters which can further characterise a BL are as follows:

- Displacement thickness (δ^*): δ^* is nothing but the reiteration of conservation of mass in a boundary layer flow. It can be defined as the distance by which the 'wall' has to be raised in a frictionless flow (no wall), in order to maintain the same volumetric flow rate as an actual boundary layer. Because of this, the streamlines outside the boundary layer would also deflect by an amount δ^* to satisfy the conservation of mass. By using control volume analysis, it can be shown that,

$$\delta^* = \int_0^{y \to \infty} (1 - \frac{\overline{u}(y)}{u_\infty}) \, dy \tag{2.1}$$

- Momentum thickness (θ): θ similarly, is used to satisfy conservation of momentum. It essentially represents a momentum loss in a BL due to the presence of the wall. Similar to the definition of δ^*, it is the distance by which the wall has to be raised in order to maintain the same momentum flow rate as in an actual boundary layer flow. By using control volume analysis,

$$\theta = \int_0^{y \to \infty} \frac{\overline{u}(y)}{u_\infty}(1 - \frac{\overline{u}(y)}{u_\infty}) \, dy \tag{2.2}$$

- Shape factor (H): It is defined as the ratio of the displacement thickness to the momentum thickness, and is independent of BL thickness δ. It gives a measure of the velocity profile shape; typically laminar BL have $H \approx 2.5$ and TBL have $H \approx 1.3 - 1.4$.

Often, one of the most important dimensionless parameter that governs a BL flow is the Reynolds number (Re). Re_x based on the streamwise distance x can be defined as $Re_x = \frac{\rho u_\infty x}{\nu}$, where ρ is the density and ν is the kinematic viscosity of the fluid. At higher free stream velocities, and therefore higher Re, the effect of viscosity is restricted to a smaller vertical extent, and thus δ is comparatively small. Due to infinitesimal perturbations that may exist in the free stream or due to surface roughness, the laminar BL transitions to a TBL which possesses a property of enhanced mixing of mass and momentum (see Figure 2.2).
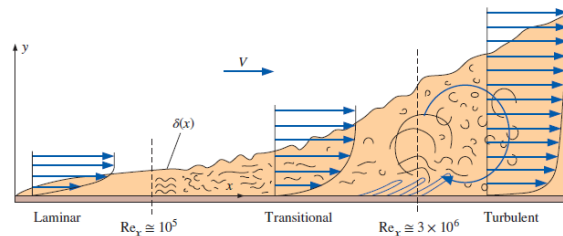
Figure 2.2: Schematic of transition from a laminar BL to a TBL on a flat plate where V is the free stream velocity (not to scale) (from Çengel et al. (2018))

2.1.2. Turbulent Boundary layers

The enhanced mass and momentum transfer across a TBL can be attributed to the presence of turbulent eddies, whereas comparatively, a lower degree of mixing takes place through viscous diffusion in a laminar BL. There is a continuous cycle of transfer of high momentum fluid towards the wall and low momentum fluid away from the wall known as sweep and ejection events respectively (more discussion in section **2.1.3**), and this effect can be observed in the turbulent velocity profile as shown in Figure **2.3**. A fully developed TBL has essentially higher gradients near the wall, and is said to be "fuller" compared to a laminar BL. The presence of higher gradients results in a higher wall shear stress τ_w given by,

$$\tau_w = \mu(\frac{\partial u}{\partial y})_{y=0} \tag{2.3}$$
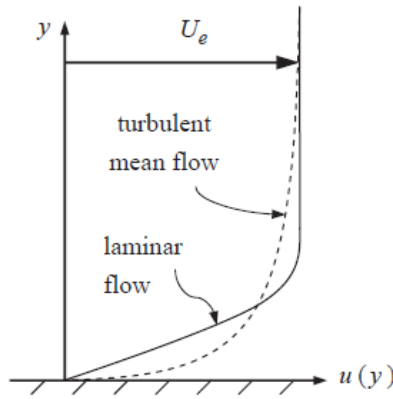
Figure 2.3: Laminar and turbulent velocity profiles (Nieuwstadt et al. (2016))

Different scaling regions can be identified in a ZPGTBL owing to its self-similarity property. The length and velocity scales used depend on the distance from the wall, and are classified as the inner and outer regions. The inner region is dominated by viscous effects, and the inner variables used for scaling are ν and u_τ, where u_τ is the wall-friction velocity defined as $u_\tau = \sqrt{\frac{\tau_w}{\rho}}$. Whereas in the outer layer, the relevant length and velocity scales used are the BL thickness δ and the free stream velocity u_∞ respectively. The inner normalised length and velocity scales are shown in equation 2.4.

$$y^+ = y\frac{u_\tau}{\nu} \qquad U^+ = \frac{\bar{u}}{u_\tau} \tag{2.4}$$

Apart from the inner and outer regions, a wall-bounded turbulent flow can be further divided into different scaling regions depending on the distance from the wall as shown in Figure **2.4**. An overlap region also known as the inertial sublayer exists which essentially matches the inner and outer region. In this region, the inner normalised velocity, U^+ as a function of y^+ follows a logarithmic behaviour, and is often referred to as the 'log-law', and is valid between $y^+ > 30$ and $y \leq 0.2\delta$. In the viscous sublayer region, applicable for $y^+ < 5$, a linear variation exists between U^+ and y^+, with the buffer layer valid in the range $5 < y^+ < 30$, with no simple solution. The log-law is often expressed as:

$$U^+ = \frac{1}{\kappa}(\ln(y^+) + B) \tag{2.5}$$

where $\kappa \approx 0.41$ is the *von Karman* constant and B is another constant.
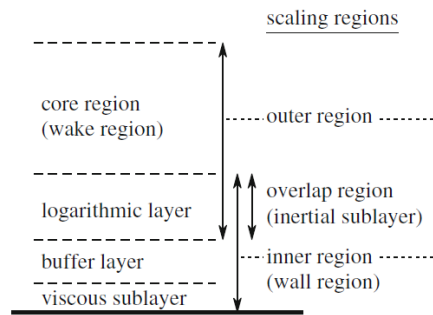
Figure 2.4: Scaling regions in a wall turbulent flow (Nieuwstadt et al. (2016))

Often, turbulent motion is associated with being complex and random, though many studies of late have demonstrated the existence of organisation amongst this randomness through the presence of coherent structures, which is the focus of the next section.

2.1.3. Coherent structures in Turbulent flow

Coherent structures are considered to be the building-blocks of turbulent flows. These coherent motions are mostly responsible for the turbulent kinetic energy (TKE) production and the maintenance of turbulence in the BL, and hence a study of these structures might be of importance in understanding the dynamics of a TBL. A majority of studies until now have posited different qualitative understandings on coherent motions based on visualisations of a TBL flow, owing to different measurement techniques used. The following discussion will try to give an idea on the currently accepted view on the characteristics of these elementary structures, although an in-depth treatment is necessary to appreciate the physics behind these flows which is beyond the scope of this thesis.

Near wall low-speed streaks

One of the earliest discoveries of coherent structures was that of low-speed streaks by Kline et al. (1967) (see Figure **2.5**). They are characterised by elongated regions of low-speed fluid oriented in the streamwise direction, with a spacing of about 100 viscous units between streaks. One of the most important features associated with low-speed streaks is the bursting process, which accounts for most of the TKE and Reynolds shear stress (RSS) produced, and involves the lift-up of streaks, oscillations, stretching and finally breakup. This event was later shown to be a sequence of ejection events with increasing strength (Tardu (1995)).
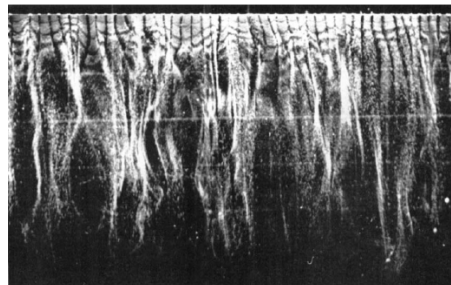
Figure 2.5: Hydrogen bubble visualisation of low-speed streaks at $y^+ = 2.7$; flow from top to bottom (Kline et al. (1967))

Vortical structures

The concept of a horseshoe vortex was first proposed by Theodorsen (1952). His model was visualised/conceptualised based on a vortex element oriented spanwise to the mean flow being stretched

by shear into hairpin loops (see Figure **2.6**). This individual hairpin vortex is considered a coherent structure. Horseshoe vortices, also called hairpin vortices, can be symmetric or asymmetric depending on the stage of evolution they are in. The heads of these hairpins which is arch shaped, lie at higher wall normal positions and thus are convected at higher mean velocities compared to its neck and legs (see Figure **2.7** for geometry). This leads to stretching of the vortex, ultimately leading to an intensification of its vorticity.
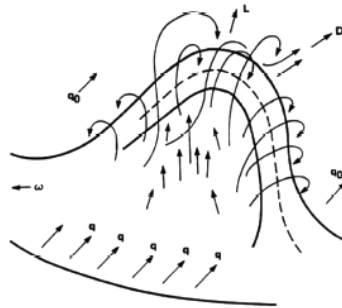
Figure 2.6: Model of a horseshoe vortex (Theodorsen (1952))
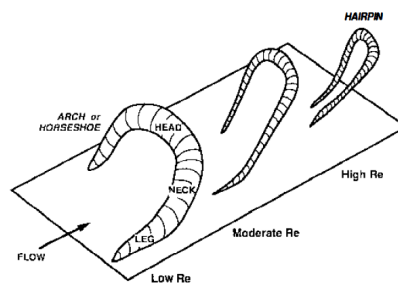
Figure 2.7: Geometry of hairpin vortical structures (Head et al. (1981))

Quasi-streamwise vortices are often represented as the legs of hairpin vortices spaced at about 100 viscous lengths apart, and form another class of coherent structures. They are predominantly aligned in the streamwise direction, although often tilting at an angle, hence its name. These vortices mostly populate the buffer layer and cause ejection (also known as $Q2$ event) of low speed fluid upwards through vortex induction between the legs of hairpin vortices, and are often associated to the formation of low-speed streaks (though still remains an open discussion). An ejection event is followed by a sweep event (also known as $Q4$ event) with an in-rush of high speed fluid towards the wall. As a result of these two events, an inclined shear layer at about $45°$ to the streamwise direction is formed, which rolls up to spawn another vortex head with spanwise vorticity.
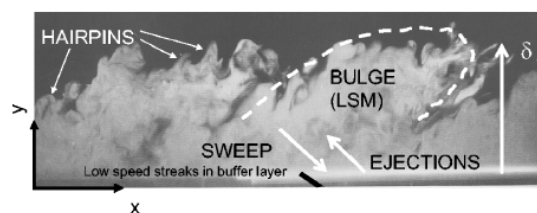
Figure 2.8: Smoke visualisation of xy plane in a TBL showing LSMs (Falco (1977); Adrian (2007))

The quantification of Reynolds shear stress (RSS) is done using quadrant analysis in the u'-v' space. They are classified into: $Q1$ events ($u' > 0$ and $v' > 0$); $Q2$ events ($u' < 0$ and $v' > 0$); $Q3$ events ($u' < 0$ and $v' < 0$); $Q4$ events ($u' > 0$ and $v' < 0$); $Q2$ and $Q4$ events are known as ejection and sweeps respectively, and are the main contributors to the RSS and hence the turbulent kinetic energy (TKE) production.

Secondary, tertiary and even downstream hairpin vortices can spawn from a single hairpin vortex through vortex induction, leading to a streamwise alignment of these vortices to form a hairpin vortex packet with limited dispersion between the vortices (Head et al. (1981); Adrian et al. (2000);). This auto-generation mechanism of hairpins might possibly give further insight into the self-sustaining property of turbulence. Further, internal shear layers separating zones of uniform momentum are often created in hairpin packets known as uniform momentum zones (UMZs) (Adrian et al. (2000)).

These hairpin packets can extend beyond the log layer till the edge of the BL and form bulges or large scale motions (LSM), that can have length scales of the $\mathcal{O}(2 - 3\delta)$ (interpretation shown in Figure 2.8). The outer layer is generally populated with many scales dominated by spanwise vorticity, with the LSMs responsible for entraining irrotational fluid. Another class of coherent structures are the Very large scale motions (VLSM) or superstructures observed mostly in the lower wake region, and are associated with the streamwise concatenation of multiple hairpin packets with length scales of the $\mathcal{O}(10\delta)$. The outer layer is said to have a modulating effect on the inner layer where most of the TKE is produced, though this is said to be Re dependent (Robinson (1991)). In conclusion, there's still active research dedicated to the study of these elementary structures which might help in obtaining a better and coherent perspective of turbulence.

2.2. The ALDR technique

This section intends to give an overview of relevant studies pertaining to the current research topic, with an aim of formulating the scope of this thesis. The active drag reduction technique of air layer drag reduction (ALDR), involves the injection of air below a solid surface (most commonly a ship hull). At a critical air flow rate, a cushion of air (known as an air layer) separating the solid surface of the hull and the high density fluid below (water) is formed. The interdependence between the surrounding flow and the air layer has not yet been widely explored, particularly the TBL development beneath the air layer and this is the focus in the current study.

2.2.1. TBL beneath an air layer
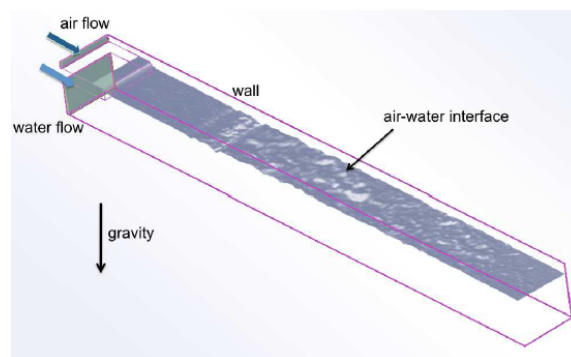
(a)

Figure 2.9: See next page for description.

(b)
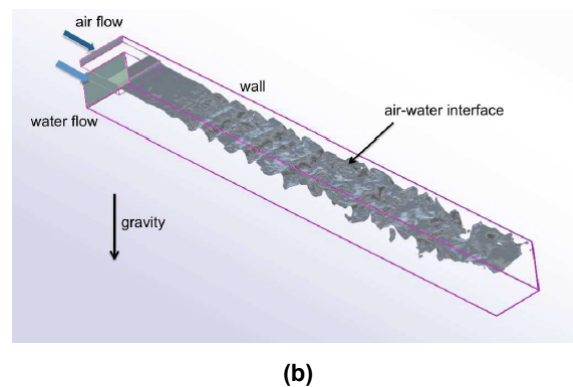
Figure 2.9: Stability of air-water interface determined by the air flow rate : (a) Stable air-water interface at high air injection rates (b) Unstable air-water interface at low air injection rates. Instability seen developed due to KH instability (Kim et al. (2010)).

Using Direct numerical simulation (DNS), Kim et al. (2010) studied the stability of an air layer over a backward-facing step. They found that at high air injection rates, Kelvin-Helmholtz (KH) instabilities were suppressed and the amplitude of disturbances decayed downstream. This lead to a stable air layer, thus leading to a reduction in skin friction. On the other hand, at air injection rates lower than a critical value, the KH instability could not be suppressed, causing water to penetrate into the air layer and thus coming in contact with the wall. This water patch grew downstream promoting the breakup of the air layer, and thus increasing skin friction (see Figure **2.9**) (Kim et al. (2010)).

A recent study by Martinez de la Cruz (2019) focused on the mechanism by which super-hydrophobic surfaces (SHS) prevent air layer breakup under turbulent conditions beneath the air layer. He studied the deformations subjected to the air-water interface by turbulent fluctuations (due to the water TBL), and solved the interface shape as a function of space and time. Based on the turbulent conditions studied, the fluctuations seemed to provoke the air layer collapse by protruding into it and thus making contact with the wall, leading to liquid entrainment. Pressure fluctuations induced by turbulence were used as an input to determine the interface shape, but were approximated from those of a channel flow case, and thus didn't portray an accurate description of the interface.

(a) External protrusion called cavitator below flat plate

(b) Principle of injection
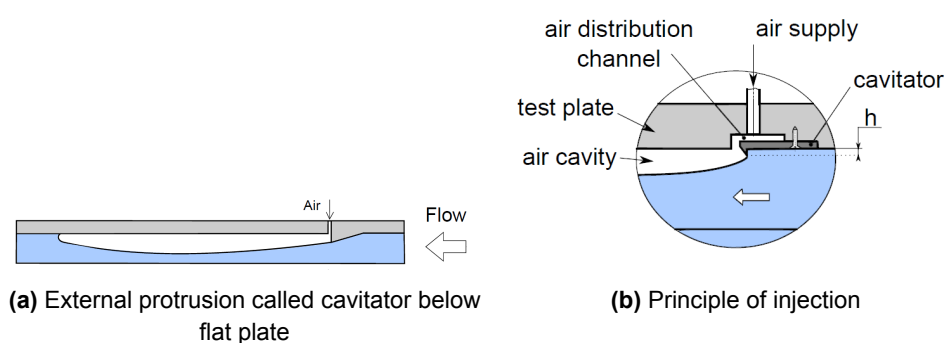
Figure 2.10: Lubrication using air cavity technique (Zverkhovskyi (2014)).

An air cavity based parametric study on the influence of inflow conditions was done by Zverkhovskyi (2014). The air cavity lubrication differs from the air layer lubrication of the current study (for ref. see Figure **1.2**) in that an external protrusion called a cavitator is used, resembling a backward facing step, behind which the air is injected (see Figure **2.10**). This method of air injection is found to be more stable compared to the air layer setup, but has a disadvantage of perturbing the incoming liquid flow due to

the obstruction created, as well as incurring higher installation costs.

It was shown in the study by Zverkhovskyi (2014) that parameters such as cavity length and thickness were crucial to achieve drag reduction. The cavity length and thickness were found to be dependent on inlet conditions such as the liquid velocity and turbulence intensity (TI). The air-water interface was shown to be more resistant to small-scale waves when the thickness of the air cavity was on the same order or slightly thicker than the incoming TBL, that is when the air injection took place near the test section inlet and the TBL didn't develop for a sufficient streamwise distance. On the other hand, when the injection was done further downstream and the ratio of the TBL thickness to the air cavity thickness was high, the waves generated at the interface were much stronger owing to higher turbulent fluctuations, thus further decreasing the cavity length. However, such observations still lack a clear physical interpretation.

Further, Zverkhovskyi (2014) also extracted average velocity profiles of the TBL at three different positions for the case when the point of injection was sufficiently downstream such that $\delta \approx 2t_{max,air}$, where $t_{max,air}$ is the maximum thickness of the air cavity (see Figure **2.11**).
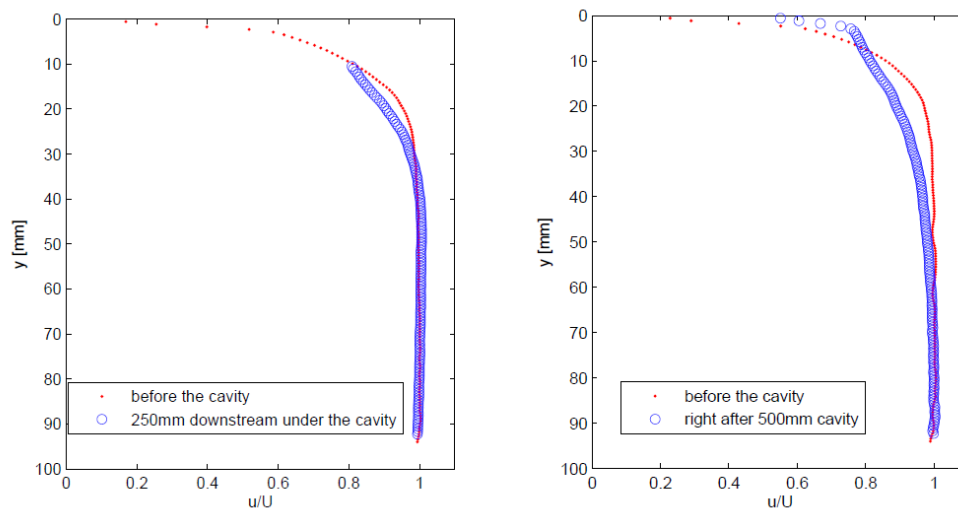
Figure 2.11: TBL under an air cavity. Here, u is the averaged velocity normalised by U which is the free-stream velocity of $1.25\ m/s$ in this case; $y = 0$ is at the wall (Zverkhovskyi (2014)).

The region preceding the air cavity is nothing but a single-phase canonical TBL (shown in red), compared with the profiles at the middle of the cavity (a two-phase flow) and at the end of the cavity, where the profile seemed to be reverting back to its canonical state. Though these plots clearly show the influence of the air injected and the interface on the TBL, further investigation is necessary to get a clearer picture of their interdependence.

To sum up, in the above mentioned studies (Kim et al. (2010); Martinez de la Cruz (2019); Zverkhovskyi (2014)), there has not been much insight into the influence of the air-water interface on the TBL developing underneath it particularly with respect to TKE production, RSS etc. Initial conditions are known to alter the behaviour of the TBL below the cavity which in turn affects the stability of the interface. However, these effects are not yet clear or studied in detail and further research is needed to reveal the intricacies of this interdependence. Quantitative measurements of the TBL below the air cavity, which are scarce in literature might help shed more light into these phenomenon and this is one of the main objectives of this thesis.

Another region of interest in the flow that has received considerably less attention is the point where the incoming TBL meets the injected air entering into the liquid cross-stream (for illustration, see figure **2.12**).
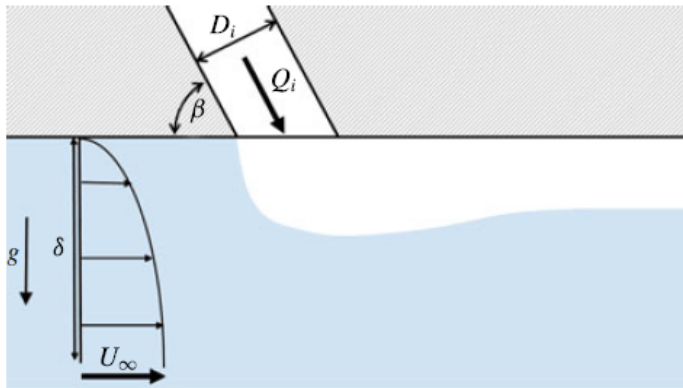
Figure 2.12: Side view of gas injected at flow rate Q_i, from an orifice diameter, D_i at an angle β to the liquid cross-stream. The free-stream velocity of the liquid is u_∞ with the BL thickness δ (Mäkiharju et al. (2017)).

Mäkiharju et al. (2017) studied numerically and experimentally the influence of a liquid cross-stream flow on the topology of gas jet injected from a single nozzle with the schematic as seen in **2.12**.
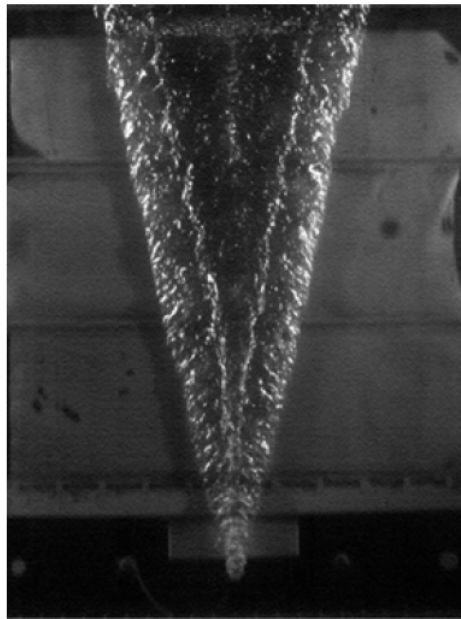
Figure 2.13: Flow topology when viewed from below, with air filled between the two branches of the "V" (so called Delta topology). Here u_∞ is from bottom to top (Mäkiharju et al. (2017)).

As a result of using a single-point injection system rather than a spanwise slot to distribute the air uniformly along the span, the gas jet was seen to bifurcate into a V-shape (see figure **2.13**) at a short streamwise distance from the point of injection, while rising to the plate surface due to buoyancy. The cavity in between the two branches of the "V", was either filled with the liquid or air (the latter forming a continuous air layer along the span) depending on u_∞. The impingement of the oncoming liquid flow on the gas jet resulted in a stagnation point at the point of contact, with the gas jet being deflected in

the downstream direction. In addition, the momentum induced due to the injection of air played a role in modifying the liquid BL. The topology of the gas jet downstream was also observed to be influenced by u_∞ and δ at the point of injection. This basically points to the interdependence of the air cavity and the TBL. It is intuitively expected that the modification of the TBL due to the hindrance of the air layer, might possibly alter the well-known coherent structuring of a TBL.

The flow geometry of a TBL flow below an air cavity is in some ways similar to studies in literature of flows over solid bumps. An experimental study on boundary layer flow over a two-dimensional curved hill was performed by Baskaran et al. (1987) (see figure **2.14**). The boundary layer was subjected to a short concave region followed by a prolonged convex region, with pressure gradients changing from adverse to favourable and then back to adverse as a result of the curvature. The ratio of the upstream boundary layer thickness to the height of the bump (δ/h) was 0.25, and as a result the boundary layer was observed to separate on the leeward side of the hill. Further, the authors reported the formation of an internal layer within the boundary layer due to the curvature change from concave to convex. The stresses were observed to increase within the internal layer as it grew, while the outer region displayed a gradual decrease in stresses which was attributed to the prolonged convex streamline curvature.
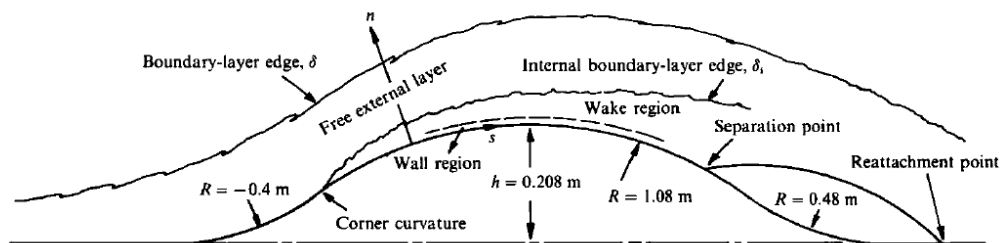
Figure 2.14: Illustration of turbulent flow over two-dimensional curved hill in the study of Baskaran et al. (1991).

A similar experimental study was performed by Webster et al. (1996), where the ratio δ/h was 1.5. In this case, the BL was not seen to separate in the leeward side of the bump. Two internal layers were observed to be formed; first at the discontinuity in surface curvature at the concave-convex region and second, at the transition from convex curvature to flat surface (similar to the flow geometry in figure **2.14**). They were observed by knee-points in stress profiles. The remnants of the upstream BL meanwhile, appeared to decay downstream. Interestingly, the outer region in this study compared to Baskaran et al. (1987) was relatively unaffected indicating that the influence of streamline curvature was not very important. Studies by So et al. (1973) and So et al. (1975) found the effects of streamline curvature to be restricted to the outer region of the TBL. Boundary layer flow over a concave curvature had a destabilising effect resulting in an increase in TI and wall-normal transport of momentum (So et al. (1975)), whereas flow over a convex curvature led to a stabilising effect on the BL resulting in a decrease in stresses (So et al. (1973)).

At the other end of the spectrum (at high δ/h ratios), Jackson et al. (1975) theoretically studied turbulent wind flows (atmospheric BL) over low hills ($\delta \approx 10h$) resembling meteorological flows. The authors reported the height of the hill (h) and the curvature effects to not produce a large disturbance to the boundary layer. Overall, the changes to the inner region of the TBL were found to dominate the flow behaviour.

The TBL in the above studies of Baskaran et al. (1987) and Webster et al. (1996) was subjected to perturbations in the form of streamwise pressure gradients and streamline curvature introduced by the curvature of the solid bump. However, TBLs in general can be subjected to other perturbations as well such as changes in surface roughness, in the application of suction or blowing or even by a

combination of the above mentioned perturbations. To gain more insight into the response of TBLs to sudden change in boundary conditions, Smits (1985) reviewed the behaviour of TBLs subjected to various abrupt perturbations. The effect of perturbations was seen to depend on their strength and the distance over which they were applied. Further, the extent of their effect within the BL (either from the inner or outer region), and the response time of the flow parameters also played a role in that influence. Streamwise pressure gradients initially affect the inner region and then spread to the outer region in the form of internal layers. Internal layers are known to be triggered when there is a sudden change in boundary condition such as the presence of wall roughness, streamline curvature or pressure gradients, which modifies the flow due to changes in the velocity gradient and turbulent stresses. Extra strain rates induced by streamline curvature on the other hand, had their strongest non-equilibrium effect on the outer region of the TBL as seen previously.

TBLs subjected to pressure gradients are generally characterised by two non-dimensional parameters: the acceleration parameter $K = \frac{\nu}{U_e^2}\frac{dU_e}{dx}$, where U_e is the local external velocity and the Clauser parameter $\beta = \frac{\delta^*}{\tau_w}\frac{dP}{dx}$ where δ^* is the displacement thickness and τ_w is the wall shear stress. Flows under acceleration due to a favourable pressure gradient experience an attenuation in stresses due to the stabilising effect of favourable pressure gradients. At high accelerations, the TBL can undergo a reverse transitional process to reach a quasi-laminar state (Narasimha et al. (1979)). The threshold at which this process starts is based on K, which was reported by Narasimha et al. (1979) to be 3×10^{-6}. A significant deviation above the log-law was observed with a reduction in the wake region. A transition back to a turbulent state is marked by an increase in turbulence intensity (TI). TBLs subjected to adverse pressure gradients on the other hand, have been observed to display an increased wake with a shortening of the logarithmic region, and the mean velocity dipping below the classic log-law (Monty et al. (2011); Harun et al. (2013)). When scaled in inner units, the streamwise TI was observed to amplify particularly in the outer region owing to increased large-scale contributions.
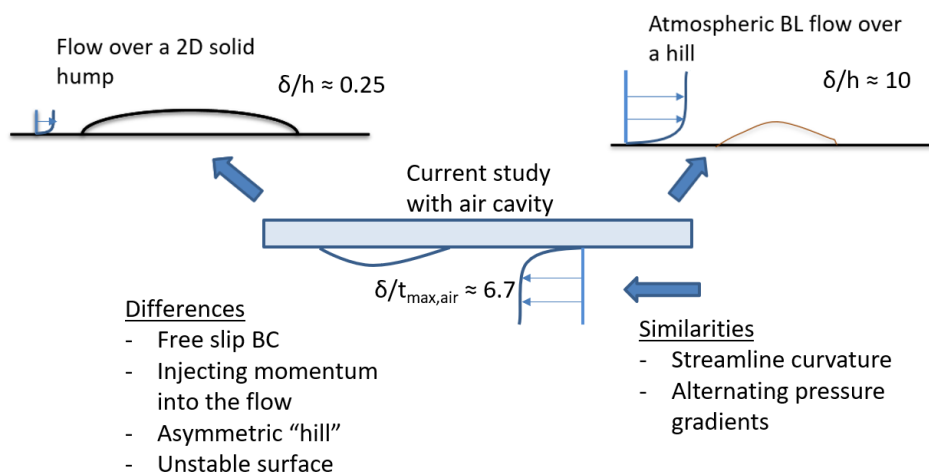
Figure 2.15: Illustration of differences and similarities of the current study with studies of Baskaran et al. (1987) and Jackson et al. (1975) with similar flow geometries. Here $t_{max,air}$ is the maximum thickness of the air cavity and h is the maximum height of the hump or hill.

To summarise, figure **2.15** shows an overview of the features of the flow in the current study in comparison with the experimental study of flow over solid bump (Baskaran et al. (1987)) and the theoretical study of an atmospheric boundary layer flow over a hill (Jackson et al. (1975)). In addition to the perturbations of streamline curvature and streamwise pressure gradients, the presence of a free-slip boundary condition along with an unstable air-water interface in the current study, makes this a much more complex flow than those mentioned above.

2.2.2. TBL below an air-water interface in the form of a free-surface

A TBL transitioning from a flat plate to a free-surface has similarity in flow dynamics with the concept of ALDR, in that a TBL encounters an air-water interface. The experimental work of André et al. (2015) touched upon the relaxation of a laminar boundary layer ($Re_\theta = 140 - 170$) as the flow transitioned from a no-slip to a free-shear boundary condition. Due to this abrupt transition from a flat plate to a free-surface, an inflection point was observed to develop in the boundary layer profile resulting in a shear layer roll-up followed by the advection of vortices. Their work mostly emphasised on trying to correlate the vortices with the deformations observed at the interface through PIV and planar laser-induced fluorescence (PLIF). They were able to relate the steepness observed in the crests and troughs of the waves to the primary vortices (from the roll-up) and the secondary vortices in the vicinity of the interface, which combined to form a counter-rotating vortex pair (CRVP) (see Figure **2.16**). These secondary vortices were generated and diffused into the bulk as a result of the high surface curvature of the interface.
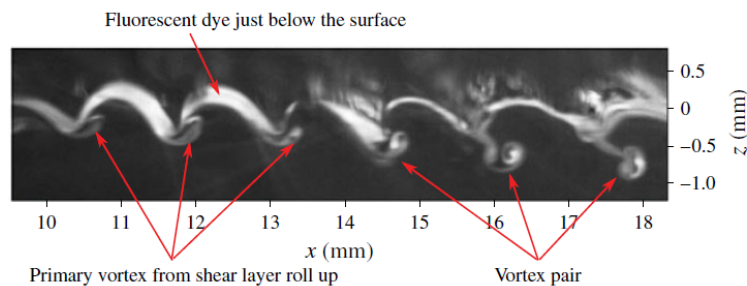
Figure 2.16: A processed PLIF image at $Re_\theta = 197$ showing flow structures below the free-surface with some reflections seen above the surface (André et al. (2017)).

It is important to note that, the response of a TBL to the change in boundary condition from a no-slip to a free-slip in the free-surface situation is not expected to be the same as when a TBL impinges an air cavity. Further, it must be kept in mind that curvature (as seen in solid bump studies) induces additional perturbations, and hence the non-linear response of the TBL would be different. On the other hand, it can give an idea how the same change in boundary condition (no-slip to slip) implemented in another form, affects the development of a TBL.

2.3. Summary of previous works and current objectives

The previous sections have briefly given an overview on the relevant studies pertaining to the current research topic. A coherent summary of these studies will aid in picking out the key takeaways, and will further help in defining the scope and objectives of this thesis.

2.3.1. Observations from previous studies

The ALDR technique involves the injection of air beneath a solid surface (most commonly a ship hull). The stability of the air layer was found to be not only dependent on the air flow rate, but also on the conditions of the incoming TBL. The influence of the air-water interface on the turbulent flow was observed in the study by Zverkhovskyi (2014) albeit very briefly. Moreover, there was no physical explanation to the link between different initial free-stream conditions and the observed behaviour of the air cavity. This motivates us to study the boundary layer development below the air cavity so as to gain some insight into this dependence. From a fundamental perspective, studies on flow over solid bumps share some similarities in the flow geometry of flow over an air cavity. The shape of the solid bump is observed to dictate the development of the TBL, particularly the ratio of the upstream boundary layer thickness to the height of the bump. The curvature of the bump was responsible for subjecting the TBL to perturbations such as alternating pressure gradients and streamline curvature, and caused

the bifurcation of the initial BL leading to the formation of an internal layer. Pressure gradients can be stabilising or destabilising, and can bring about significant changes in the BL structure. The presence of a free-slip boundary condition along with an unstable air-water interface in addition to the perturbations discussed, makes the flow in the current study an increasingly complex flow. To sum up, a better understanding on the interdependence of the air-water interface and the turbulence below can not only help in providing a better insight into the physics of their interaction, but also in optimising this technique.

2.3.2. Current objectives

The previous sections have so far highlighted the relevant research areas with respect to the problem at hand. The aim of this thesis is to attempt to cover certain gaps observed in literature so as to improve our understanding of this unique flow. To gain better clarity of the goals for this thesis, defining an overarching research theme and posing relevant research questions is central to this purpose. To this end, the research theme can be formulated as,

"**Experimental investigation of influence of an air cavity on a turbulent boundary layer using PIV**"

with the following broad research questions to be addressed in this thesis,

- **Identification of air cavity:** An attempt will be made to identify the shape of the air cavity and detect the position of the air-water interface. It would give an idea of the role the cavity shape plays in dictating the behaviour of the surrounding flow. Further, comparisons can then be made to flow geometries observed in solid bump studies in literature to identify the differences and similarities.

- **Qualitatively and quantitatively study the development of the TBL in the presence of an air cavity:** For this purpose, planar PIV will be used to study the mean and fluctuating flow field by considering fields of view (FOV) at regions upstream and below the air cavity. To quantify the effects on the boundary layer development, mean velocity profiles and higher order statistics such as stresses of the TBL will be considered.

3

Experimental Setup and Data acquisition

This chapter discusses the basic principle of planar PIV which was used to investigate the flow. The experimental setup and specifications used to acquire raw images are described in detail. This is followed by a description of the data reduction parameters used to extract instantaneous velocity fields.

3.1. Particle Image Velocimetry

Particle Image Velocimetry is a non-intrusive optical flow measurement technique which has been gaining popularity in the last few decades as a quantitative flow visualisation tool. In comparison to other measurement techniques such as LDV or HWA, it provides an added advantage of quantifying measurements in combination with flow visualisation at a moderate spatial and temporal resolution (compared to HWA and LDA which typically operate at higher resolutions). It is a full field technique in which instantaneous velocity fields can not only be extracted in a plane (planar PIV), but also in a volume (tomographic PIV), hence making this an appealing flow measurement technique. The current research work will utilise the technique of 2C-2D (two component-two dimensional) planar snapshot PIV, and this chapter aims to focus briefly on the fundamentals of PIV and the specifications of the current experimental campaign. For an extensive insight into PIV, the reader is referred to Adrian et al. (2011) and Raffel et al. (2018).

3.1.1. Working Principle

PIV is an indirect measurement technique: the displacement of tracer or seeding particles carried by the flow is used to determine instantaneous flow fields. Initially, the flow is seeded with particles with the aim of achieving an approximately homogeneous distribution. These particles are then illuminated within a thin light sheet (for planar PIV) containing the area of interest using a pulsed light source such as a laser. The illumination is typically done in two time instances separated by a parameter known as the pulse separation time Δt, which depends on the flow velocity and on optical parameters such as the magnification. The light scattered by the tracers are captured by digital imaging devices such as Charged couple device (CCD) or Complementary metal-oxide semiconductor (CMOS). In order to evaluate the PIV images, the frames are divided into interrogation windows such that each of them contain sufficient number of particle images. A cross correlation algorithm between the two images is then used to determine the displacement of the particles based on the peak correlation obtained. Using the displacements measured, the time separation and the magnification, instantaneous velocity fields in a planar cross-section of the fluid flow can be determined. The final step involves using post-processing algorithms to identify and replace spurious vectors, and to limit the background noise, which is necessary to extract further quantities of interest. An example of a planar PIV setup is shown in figure **3.1**.
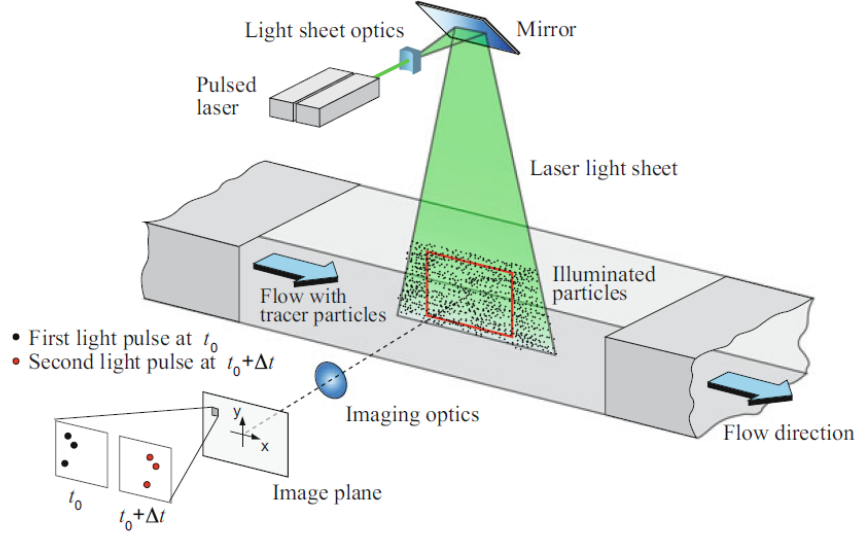
Figure 3.1: Typical experimental setup of 2D-2C PIV (Raffel et al. (2018)).

3.1.2. Seeding the flow

As stated previously, the displacement of tracer particles is used to give an indirect measurement of the displacement of actual fluid flow parcels. The most important tracer parameters that govern the sound execution of PIV measurements are the size, the seeding concentration and the optical properties of the particles. Typically, particles need to be small enough in order to follow the flow faithfully, but of sufficient size to scatter light in order to be captured by the image sensor. Thus a trade-off must be achieved between these two parameters to maintain optimal conditions for measurement. In addition, the seeding density or the concentration should not be too high to locally cause an alteration to fluid properties leading to multiphase flow effects. The seeding concentration, C usually ranges between 10^9 to 10^{12} particles per m^3 (Scarano (2013)).

The particle dynamics is mostly dominated by the Stokes' drag, and for an accelerating fluid, the velocity lag or the difference between the particle velocity ($\mathbf{V_p}$) and fluid velocity ($\mathbf{V}$) can be estimated as:

$$\mathbf{V_p} - \mathbf{V} = \frac{d_p^2(\rho_p - \rho)}{18\mu}\frac{d\mathbf{V_p}}{dt} \tag{3.1}$$

where d_p and ρ_p are the particle diameter and density respectively, and ρ and μ are the fluid density and dynamic viscosity respectively. This difference between the velocities is known as the slip velocity, and represents the "velocity lag" or the finite amount of time the particle takes to adjust to changes in the flow, which can be defined in the form of a particle response time, τ_p as shown in equation **3.2**.

$$\tau_p = \frac{d_p^2(\rho_p - \rho)}{18\mu} \tag{3.2}$$

Thus, the main aim is to minimise the response time or the slip to achieve an optimal condition of the particles following the flow faithfully. This can be easily satisfied in liquid flows using neutrally buoyant particles ($\rho_p \approx \rho$) with diameters of the order of $(10 - 100)\mu m$. On the other hand, in gaseous flows, in most cases $\rho_p >> \rho$ and due to this, smaller particle diameters are necessary such as of the order of $(1 - 3)\mu m$. Further, in addition to good tracking accuracy, the scattered light must be sufficient to make the particle visible. Mie's scattering regime typically applies when $d_p \approx \lambda$, where $\lambda = 532 \ nm$ is the wavelength of the green laser light. The scattering cross-section determines the scattering efficiency which depends on the ratio of refractive indices of the particle to the fluid ($\frac{n_p}{n}$), d_p and λ. To sum up,

a trade-off is necessary to obtain a balance between good tracking accuracy and good particle image quality.

3.1.3. Illumination and Imaging

Lasers are the typical light sources used for illumination, as they produce a pulsed, collimated and monochromatic beam of light. Solid-state lasers such as Nd-YAG (neodymium-doped yttrium aluminium garnet) are employed with an energy per pulse ranging between $20 - 500 \ mJ$. The energy intensity must be sufficient to illuminate the particles and cause light scattering to ensure adequate light captured by the sensor. The circular cross-section light beam is transformed into a light sheet by means of a cylindrical and spherical lens. This configuration (see Figure **3.2**) yields a constant-width laser sheet, with uniform illumination along the propagation direction.
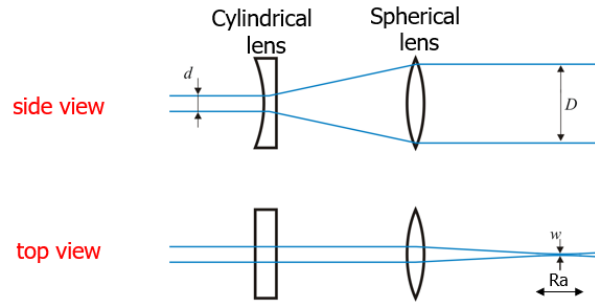
Figure 3.2: Configuration of constant-width laser sheet. d is the initial laser beam diameter; D is the final light sheet dimension; w is the laser beam waist, defined as the region where the thickness of the light sheet is minimum; Ra is the Rayleigh length, which is the length over which diffraction effects govern the light sheet thickness. (Scarano (2013))

The particle image diameter d_τ formed on the sensor is typically larger than the actual particle diameter, which can be attributed to the limits of diffraction. It can be approximated by (Adrian et al. (2011)),

$$d_\tau \approx \sqrt{(Md_p)^2 + (d_{diff})^2 + (d_a)^2} \tag{3.3}$$

where M is the magnification, d_p is the actual particle diameter, d_{diff} is the diffraction-limited diameter and d_a is particle diameter due to effects of lens aberrations. Further,

$$d_{diff} = 2.44\lambda(1 + M)f_\# \tag{3.4}$$

where $f_\#$ is the f-stop defined as $\frac{f}{D}$, in which f is the focal length of the lens and D is the lens aperture diameter. In equation **3.3**, the particle image formation is often dominated by the diffraction-limit term, d_{diff}. The optimal particle image diameter, d_τ is generally chosen to be about $2 - 3$ pixels to avoid bias errors such as peak-locking, and to increase sub-pixel accuracy (Adrian et al. (2011)). The $f_\#$ plays an important role in fine tuning the focused particle images by affecting the depth of field (DOF) observed. The DOF δz, which is the range in which particles are imaged with sufficient sharpness is given by (Scarano (2013))

$$\delta z = 4.88\lambda f_\#^2 (\frac{M + 1}{M})^2 \tag{3.5}$$

Typically, the DOF must be greater than the light sheet thickness Δz_0, for the particles to be in-focus. The source density N_S, and image density N_I, are parameters which also play an important role in the formation of good quality particle images in PIV. The source density can be defined as (Adrian et al. (2011); Scarano (2013)):

$$N_S = \frac{C\Delta z_0}{M^2}\frac{\pi d_\tau^2}{4} \tag{3.6}$$

where C is the seeding concentration. The term $\frac{\pi d_\tau^2 \Delta z_0}{4}$ represents a cylindrical volume with diameter equal to the particle image extending to a distance equal to the light sheet thickness (Δz_0). N_S basically determines whether the image plane consists of individual particle images (for $N_S << 1$) or overlapping particle images (for $N_S >> 1$). Thus a low source density is the desirable condition for PIV. The image density can be defined as the mean number of particle images in a single interrogation window and can be expressed as (Scarano (2013)):

$$N_I = \frac{C \Delta z_0}{M^2} D_I^2 \qquad (3.7)$$

where D_I is the interrogation-spot diameter. At low image densities ($N_I << 1$), individual particle tracking is possible (Lagrangian tracking) owing to very few number of particles imaged within an interrogation window. At high image densities ($N_I >> 1$), multiple particle image pairs are imaged in an interrogation window such that the displacement of a single particle image is smaller than the distance between neighbouring particle images, and thus this condition is desirable in case of PIV. Although, it is necessary to note that at high N_I, the probability of incorrect pairing of particle images also increases, with the probability of appearance of false peaks also increasing (Adrian et al. (2011)). The number of particle image pairs found at the two time instances t and $t + \Delta t$, inherently determines the performance and accuracy of PIV such that the correlation peak computed corresponds to the true particle displacement.

3.2. Experimental Setup

The PIV experiments were carried out in the Water tunnel at the Laboratory for Aero and Hydrodynamics at TU Delft. The test section of the water tunnel has a cross-sectional area of $0.6 \times 0.6 \ m^2$ and is $5 \ m$ in length (see figure **3.3**). The open surface was covered with two identical flat plates, each $2.43 \ m$ in length. The test section is made of Plexiglas to facilitate optical access. Upstream of the test section, a contraction accelerates the flow, preceded by a honeycomb and a series of screens to ensure isotropy and reduce the turbulence intensity. The water tunnel is a closed-loop type system with the flow driven by a pump and is recirculated back through a pipe that runs under the water tunnel. The flow speed is controlled through the pump frequency and can reach a maximum of $1 \ m/s$.
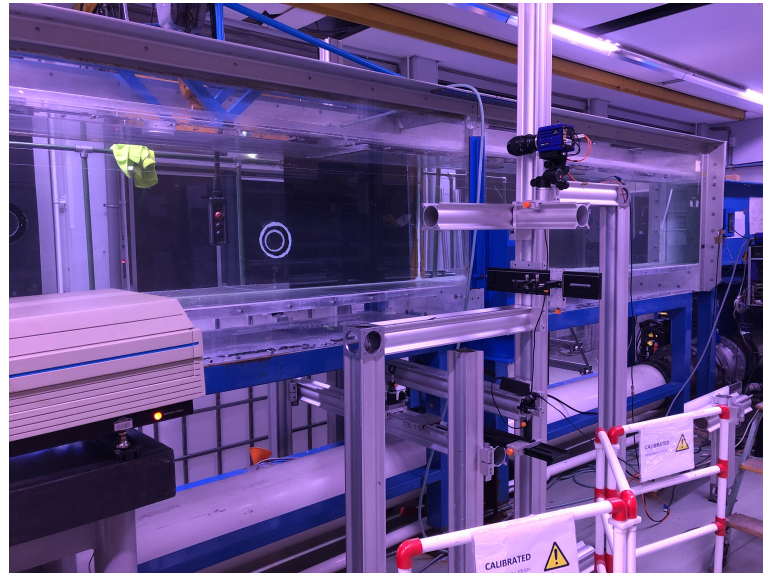
Figure 3.3: Water tunnel at the Laboratory for Aero and Hydrodynamics.

Figure **3.4** shows a schematic of the experimental setup used to study the flow with the mounted camera and sheet forming optics along with the light beam path. The flow is from right to left with the

TBL under investigation developing below the top flat plates which were used to cover the open surface of the water tunnel (refer to figure **3.5b** for illustration of the boundary layer developing). The light beam was guided underneath the water tunnel by a series of mirrors and was subsequently shaped into a thin sheet by means of cylindrical and spherical lenses. It was then directed upwards towards the measurement region in the water tunnel using another mirror. The locations for the mounting of the camera and the array of optics were strategically chosen to allow sufficient degrees of freedom and flexibility for the different measurement campaigns.
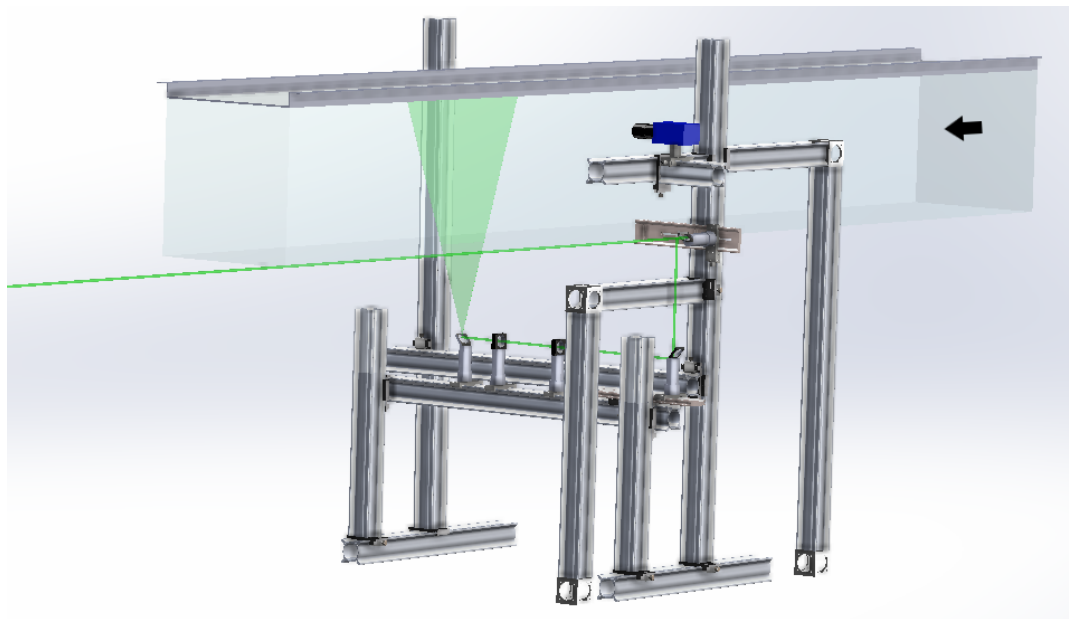
Figure 3.4: Schematic of Experimental setup to study the flow with laser path shown (in green). Arrow indicates direction of flow.

3.2.1. Injector geometry

The different air injection methods used to create an air layer (cavitators and backward facing step) were discussed in chapter **2**. For our current study, the air injector geometry shown in figure **3.5a** was used to create an air layer. A slot type injector was employed spanning the width of the second (downstream) plate, fitted at a distance of $0.5\ m$ from the leading edge of the plate. The width of the slot through which air was injected was $4\ mm$, with air being dispersed over the whole span. The injector geometry employed for this study to generate an air layer differs from the ones used in literature in that no cavitator or backward facing step was used, hence avoiding protrusions into the incoming flow. On a side note, it should be kept in mind that different air injection methods can create different air layer regimes depending on the free-stream conditions and air flow rates employed, which can affect the dynamics of the interaction between an air layer and an incoming TBL (Zverkhovskyi ([2014](#)); Elbing et al. ([2013](#))). As a result of this unique geometry, air is injected perpendicularly into the flow and as a consequence of the inertia carried by the latter, the injected air bends and reaches the surface of the plate forming an air cavity. By varying the air flow rates and the free-stream velocity, different air layer regimes such as bubbly, transitional or a continuous air layer regime can be created using this setup (reader is referred to Nikolaidou et al. ([2021](#)) for more information). For our current study, a continuous air layer regime is the desired experimental condition. Figure **3.5b** shows an illustration of the air layer formed.

(a) Air injector geometry   **(b)** Formation of air cavity
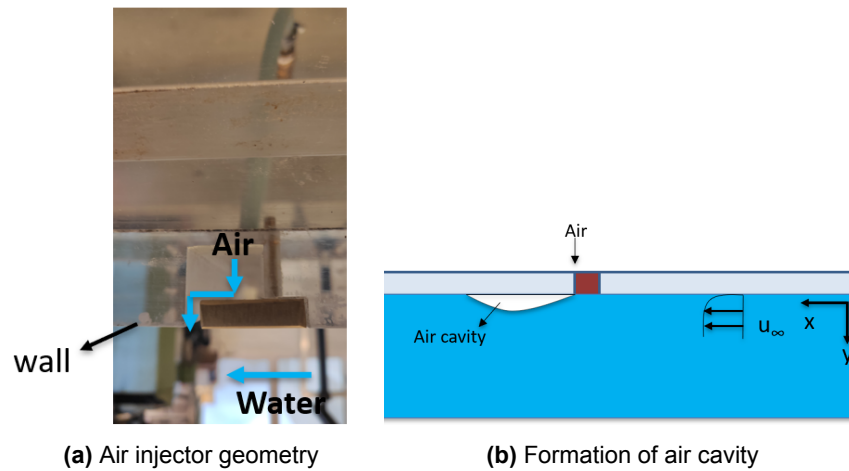
Figure 3.5: Principle of air injection.

3.3. Employed equipment and Experimental parameters

3.3.1. Employed equipment

Light source

The illumination is obtained through a double-pulsed dual-cavity Nd-YAG laser with an operating frequency of $15\ Hz$. The pulses initially generated in the infrared range ($1064\ nm$) are converted to a green light source ($532\ nm$) at the output through a frequency doubling crystal. The circular cross-section beam is shaped into a thin laser sheet in the streamwise-wall-normal direction with a thickness of about $1\ mm$ by means of a spherical and cylindrical lens, and then directed towards the desired measurement region using a mirror (see section **3.2**). The laser path is illustrated in figure **3.4**.

Imaging

The imaging is done using a low-speed scientific CMOS camera assembled by LaVision (see figure **3.6**). It has a pixel pitch of $6.5\ \mu m$, with a full resolution of 2560×2160 pixels that can be operated at a frame rate of $50\ Hz$. A Nikon objective of focal length $105\ mm$ is mounted to the camera. The synchronisation of the laser pulses and the imaging system is achieved by control through a LaVision Programmable time unit (PTU).

Figure 3.6: sCMOS camera by LaVision with $105\ mm$ focal length Nikon objective.

Seeding
Sphericell hollow glass spheres of density $0.998 \times 10^3 \ kg/m^3$ with a mean diameter of $15 \ \mu m$ are used as the seeding particles. These tracers are typically small enough to follow the flow faithfully, at the same time large enough to sufficiently scatter the laser light.

3.3.2. Fields of view
In order to study different aspects of the flow, different positions along the streamwise direction were considered, enabled by the flexibility of the experimental setup. Figure **3.7** shows an illustration of the various fields of view used. The large field of view (#1) with a comparatively lower spatial resolution encompassing the whole air layer enables one to study the development of the flow beneath the air cavity as well as get an approximate shape of the air-water interface. A similarly large field of view (#2) is considered upstream of the air layer to study its upstream influence on the incoming TBL, and also to characterise the incoming TBL at the flat plate region upstream of the injector (called the baseline TBL; more information in section **4.1**). Finally, a higher spatial resolution field of view (#3) near the injection location is used to investigate the presence of recirculation zones.
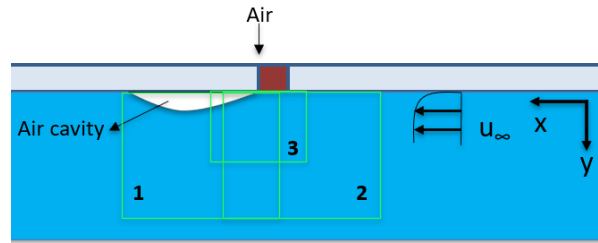
Figure 3.7: Illustration of the fields of view considered in the experimental campaign.

3.3.3. Experimental parameters
In order to ensure transition to turbulence, the flow was tripped at the inlet of the test section using a zigzag strip. Parameters such as the thickness of the trip and its placement location were computed based on observations and results by Elsinga et al. (2012). The thickness of the trip was chosen to be $0.5 \ mm$ placed at a downstream location of $0.08 \ m$ from the leading edge of the first plate. A water depth of $0.56 \pm 0.03 \ m$ was maintained during measurement campaigns.
The camera captured a FOV of about $0.2 \ m \times 0.16 \ m$ in the streamwise (x) and wall-normal (y) directions respectively. The spatial resolution obtained was 0.0739 or $87.9 \ \mu m/px$. The above mentioned FOV and spatial resolution were captured for the fields of view #1 and #2 discussed in section **3.3.2**.

Initial theoretical estimates of different experimental parameters were computed based on $d_\tau \approx 2-3$ pixels. Using equations **3.3** and **3.4**, and neglecting the effect of lens aberrations, the equation was solved for $f_\#$. Another way of setting up the f-stop is by considering that the DOF must by greater than the light sheet thickness Δz_0, to avoid out-of-plane loss of particle image pairs. Thus equation **3.5** has to be greater than $1 \ mm$ (the light sheet thickness), and on solving for $f_\#$, leads to a condition that $f_\# > 2.79$.

An initial estimate of the pulse separation time Δt was computed based on a rule of thumb of not allowing the tracers to exceed a displacement larger than $\frac{1}{4}th$ of the interrogation window size. The desired free-stream tracer displacement is $7-10$ pixels. Thus, based on the free-stream velocity and a desired displacement according to the one-quarter rule, Δt was computed to be $560 \ \mu s$. A free-stream velocity of $0.68 \ m/s$ (measured through a pitot tube) and an air flow rate of $41.2 \ l/min$ were considered for this study. These parameters were chosen based on the recent study by Nikolaidou et al. (2021), where a stable air layer regime was established at these values. The formation of a "stable" air layer

is important here because the focus is on investigating its influence on the incoming TBL. An overview of all the parameters used during the experimental campaign can be found in table **3.1**.

Pixel size	$6.5 \ \mu m$
$f_{\#}$	5.6
Magnification	$87.9 \mu m/px$
Acquisition frequency, Δt	$2.51 \ Hz$, $560 \ \mu s$
Field of view	$1.85\delta \ (x) \times 1.48\delta \ (y)$
Final interrogation window size	$24 \times 24 \ px$ with 50% overlap
Spatial resolution	31^+ units
Number of uncorrelated image pairs	1800
Free-stream velocity	$0.68 \ m/s$
Air flow rate	$41.2 \ l/min$

Table 3.1: Experimental details

3.3.4. Data processing

The raw data (an example shown in figure **3.8**) acquired in the form of images using PIV were processed using DaVis 8.2 and $10.1.2$ in order to obtain velocity vector fields. The method of cross-correlation between image pairs is used to determine the instantaneous velocity fields. The image pairs (separated by time Δt) are divided into small windows known as interrogation windows, and are then cross-correlated to yield an average particle displacement per interrogation window. Using the displacement, the velocity at each window can then be found using the pulse separation time Δt and the magnification M.
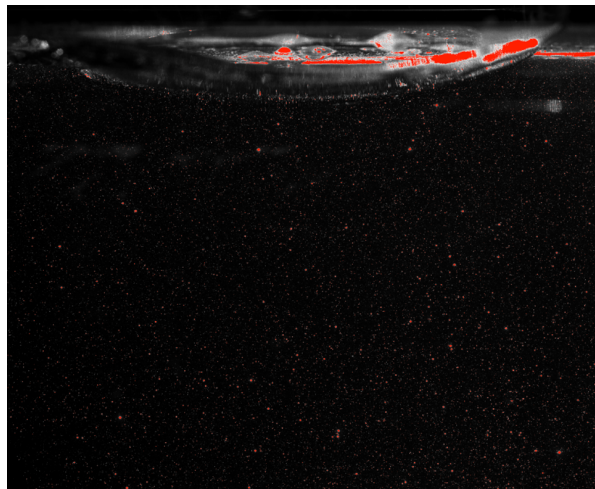
Figure 3.8: An example raw image using the field of view #1.

For our experimental campaign, a multi-pass iteration method with decreasing window size was used. An initial window size of 64×64 pixels for the first pass followed by three passes of a final interrogation window size of 24×24 pixels with an overlap of 50% was employed, resulting in a spatial resolution of 31 viscous units (note that details of this normalisation will follow in the next chapter). In order to eliminate spurious vectors, vector post-processing was performed using a median filter based on the concept of the universal outlier detection algorithm (see Westerweel et al. (2005)), followed by a filter based on a minimum correlation value of 0.4. First choice vectors accounted for almost 98% of the total vectors, thereby giving confidence in our data acquisition. To obtain statistical convergence of data, a total of 1800 uncorrelated image pairs were acquired. This was decided based on analysing the

convergence of the mean velocity and streamwise turbulence intensity (TI), using a long-time average of 2000 uncorrelated image pairs.

<div style="text-align: right; font-size: 3em;">4</div>
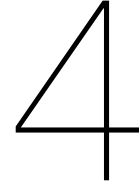
Results and Discussion

This chapter includes the results and a follow-up discussion. First, the incoming TBL is characterised followed by a discussion on the detection technique employed to identify the air cavity so as to get an idea of its shape and other characteristics. The upstream influence of the air cavity on the TBL is then evaluated, followed by the TBL development over the air cavity. The effects of the air cavity on the turbulent statistics are analysed, and finally a discussion follows on our understanding of the flow.

4.1. Baseline turbulent boundary layer characteristics

In order to assess the influence of the air layer on the development of the TBL, the characteristics of the incoming TBL before its impingement on the air layer, need to be identified. For that purpose, a measurement campaign was carried out in the flat plate region upstream of the air injector. It should be noted that this was done without air being injected to avoid any upstream influences of the air injection. To this end, the upstream FOV (FOV #2, section **3.3.2**) was used to obtain turbulent statistics such as the mean streamwise velocity and turbulence intensities (TI) of the incoming flow. The characteristics of the baseline TBL are shown in table **4.1**. The friction velocity u_τ, was estimated using a composite profile fit that fits an analytical function to the mean velocity profile valid from the wall up to the free-stream, which combines the Musker function for the inner and overlap regions, and a wake function for the outer region (Chauhan et al. (2009)). The estimate of u_τ from the composite fit was compared with the Clauser chart (Clauser (1954)) and no differences were found. Both inner and outer normalisations have been used in this study. The inner normalised velocity scale is based on the friction velocity, u_τ: $U^+ = \frac{\overline{u}}{u_\tau}$, and the outer normalised velocity scale is based on the local free-stream velocity. Similarly, the inner normalised length scale in plus units: $y^+ = \frac{yu_\tau}{\nu}$, and the length scale in outer units is based on the local boundary layer thickness. The local boundary thickness was estimated by considering the point where the turbulent stresses begin to plateau towards an approximately constant value in the free-stream.

u_∞ (m/s)	u_τ (m/s)	δ (m)	Re_τ	Re_θ
0.71	0.027	0.1085	3200	6940

Table 4.1: Baseline TBL characteristics.

To check for the canonical behaviour of the incoming TBL, the mean streamwise velocity and TI were compared against experimental studies performed at higher and lower friction Reynolds numbers ($Re_\tau = 2820$ and $Re_\tau = 4300$). The mean streamwise velocity and TI are scaled using inner (viscous) units. Figure **4.1** shows the inner-scaled mean streamwise velocity profile as a function of y^+ compared with Laser Doppler Anemometry (LDA) data at $Re_\tau = 4300$ (DeGraaff et al. (2000)).

<div style="text-align: center;">27</div>
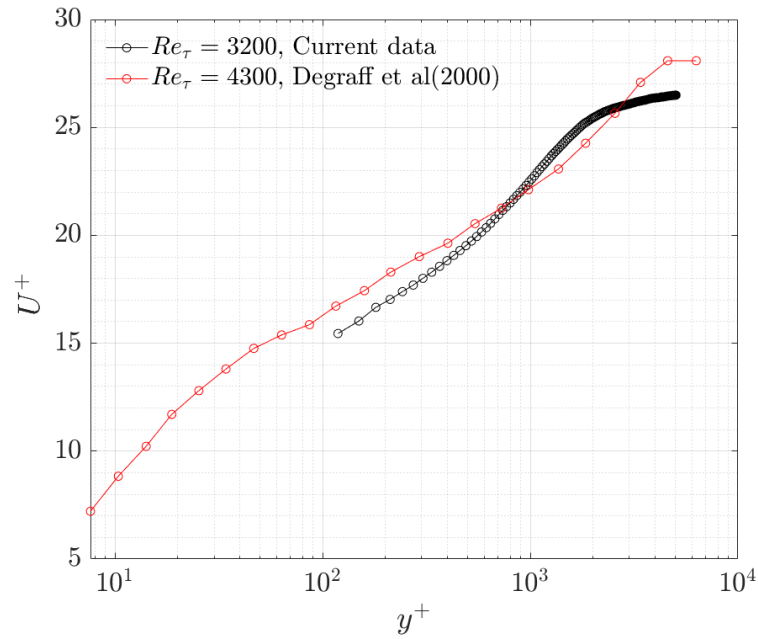
Figure 4.1: Inner normalised mean streamwise velocity profile ($Re_\tau = 3200$) shown in black compared with LDA data, DeGraaff et al. (2000) ($Re_\tau = 4300$) shown in red.
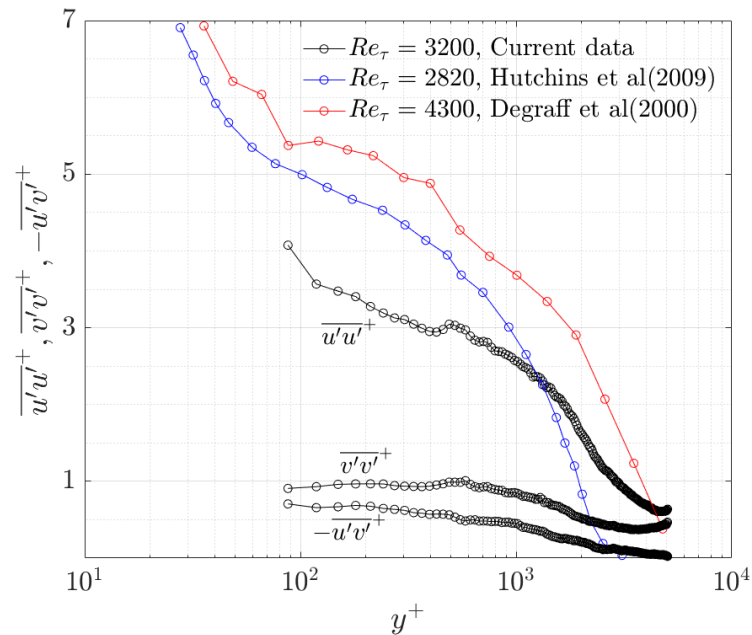
Figure 4.2: Inner normalised TI profiles of streamwise and wall-normal velocity components, and the Reynolds shear stress ($Re_\tau = 3200$) shown in black. Comparison of streamwise TI with hot-wire data, Hutchins et al. (2009) ($Re_\tau = 2820$) shown in blue and LDA data, DeGraaff et al. (2000) ($Re_\tau = 4300$) shown in red.

The region below $y^+ = 100$ including the viscous sublayer and the buffer layer could not be resolved owing to the difficulty in getting close to the wall as a result of the experimental technique being used. The logarithmic behaviour in the current study does not seem to agree very well with the LDA

measurements. In addition, the wake region does not appear to be well-formed and can be explained as result of a more than expected noisy free-stream, in addition to increased turbulence intensity due to measurements done in a water tunnel (as compared to a wind tunnel).

The inner normalised streamwise and wall-normal TI along with the Reynolds shear stress (RSS) at $Re_\tau = 3200$ is shown in figure **4.2**, along with data from literature: hot wire data from Hutchins et al. (2009) ($Re_\tau = 2820$) and LDA data by DeGraaff et al. (2000) ($Re_\tau = 4300$). There is an underestimation in the streamwise TI which was also observed for the wall-normal TI and the RSS (not shown here) compared to experimental measurements in literature. Multiple experimental campaigns were carried out to conclude that this was in fact the behaviour of the incoming TBL observed. We think this might be attributed to the imperfections observed in the experimental setup such as tiny air bubbles advecting from the contraction and a small air gap at the junction of the upstream and downstream plates. In addition, the wall-normal TI does not appear to reduce to zero in the free-stream, instead, it is seen to increase, highlighting some turbulent activity in the free-stream. To an extent, this can also explain the absence of a well-defined wake in the mean velocity profile.

The observed behaviour indicates that this TBL is not strictly canonical, albeit from an application point of view, we do not expect a canonical TBL to develop underneath a ship's hull due to multiple perturbations from various sources. Thus, this behavior is not expected to influence the results as the main aim is to understand how the air cavity affects the development of the incoming TBL.

4.2. Detection of the air-water interface

Earlier studies on flow over solid bumps (Baskaran et al. (1987), Webster et al. (1996)), showed that the shape of the bump plays a crucial role in the way the TBL behaves as it moves over it. The height and length of the bump particularly, were important parameters to the turbulent flow development on the windward and leeward sides of the bump. The flow geometry in the current study is similar to the studies on flow over solid bumps (Baskaran et al. (1987),Webster et al. (1996)) in some ways; given the observed stability of the air cavity shape over time (particularly the upstream half of it), we expect its shape to influence the development of the TBL. In light of this, we employed a detection technique to first obtain an approximate interface shape, and get an estimate of the maximum thickness and length of the air cavity which might be useful for further research in studies employing air layers for drag reduction.
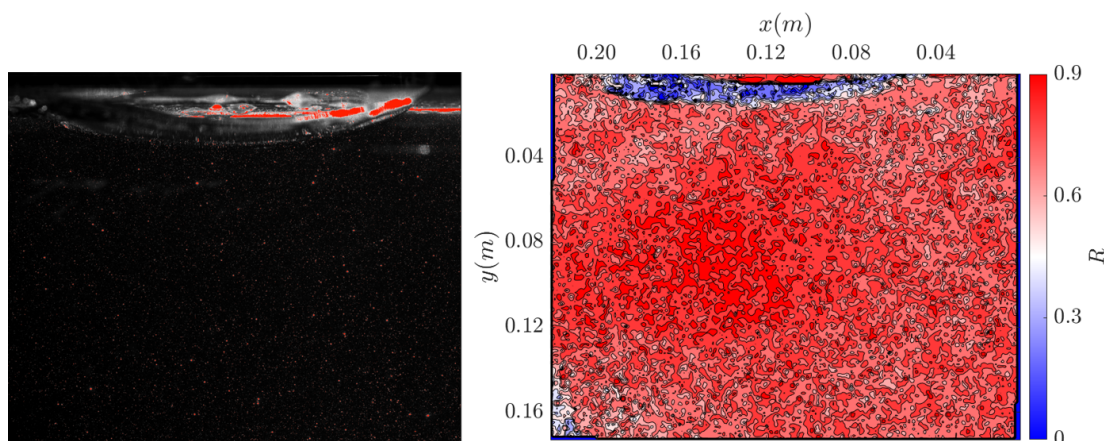
Figure 4.3: An instantaneous raw image with its corresponding correlation map using FOV #1

Interface detection techniques usually rely on methods such as gray-level intensity gradients within

an image in combination with an additional profiling camera (in addition to a PIV camera) such as in the study of Mukto et al. (2007). Sometimes, fluorescent dye may also be used in addition to seeding particles to improve the accuracy of detection by capturing different wavelengths of light scattered. However, with the employment of these techniques, there is an increase in the level of experimental complexity such as with the usage of an additional profiling camera which brings with it additional calibration procedures. Further, the detection of the air-water interface for our study using a threshold based on gray-level intensity gradients within the raw image, was not feasible owing to the small gray-level intensity gradients present near the air cavity (for example see figure 3.8). Therefore, for this study we employed a detection technique based on correlation values obtained after image post-processing. A typical instantaneous correlation map across the FOV (#1) with the corresponding raw image is shown in figure 4.3. A clear jump can be seen in the correlation values at the top of the FOV where the air cavity is present. This enables us to exploit this jump to obtain an approximate shape of the air cavity which is the next topic of discussion.

4.2.1. Detection threshold and mean air cavity shape

A threshold is necessary to separate regions which are part of the air cavity from those of the surrounding flow. An average correlation map based on all ensembles was used to obtain a threshold value, R_{th} (see figure 4.4a). This threshold value was then applied to every instantaneous image and a binary map was constructed based on the correlation values with respect to the threshold, R_{th}. For instance, an instantaneous correlation value below the threshold is assigned a logical value of 1, and hence part of the interface; similarly, an instantaneous correlation value above the threshold is assigned a logical value of 0, and hence is not part of the interface. The coordinates of a continuous interface for every instantaneous image were then extracted and averaged out to yield the mean interface position. The threshold value from the average correlation map was chosen based on multiple iterations of different threshold values and visual inspection of the raw images. Based on this, a R_{th} of 0.68 was obtained and is used for the rest of the analysis.

(a)
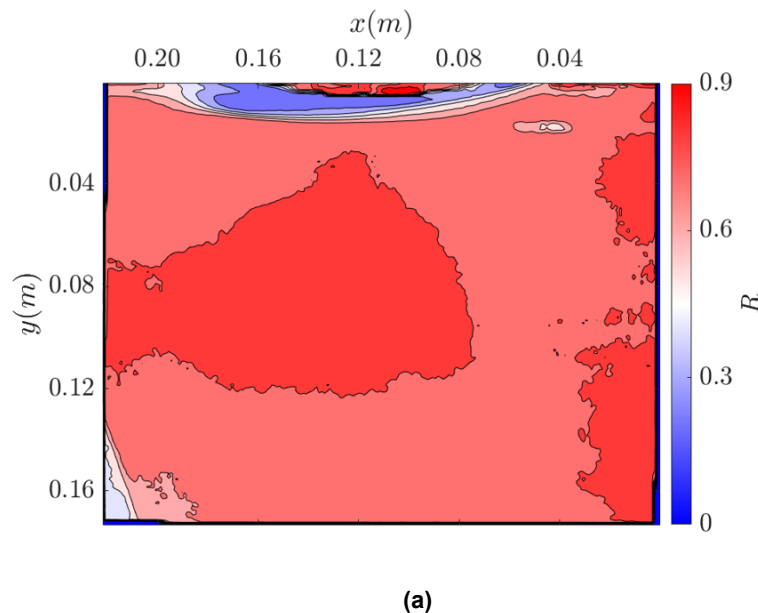
Figure 4.4: See next page for description.

The contour of the mean streamwise velocity is shown figure **4.4b** with the mask of the mean air cavity shape. The mean cavity shape reveals an asymmetric bump with a shedding region observed at the end of the air cavity, which was expected owing to the unstable nature of the cavity end. The TBL developing over the flat surface impinging on the air cavity, experiences a prolonged convex region

(b)
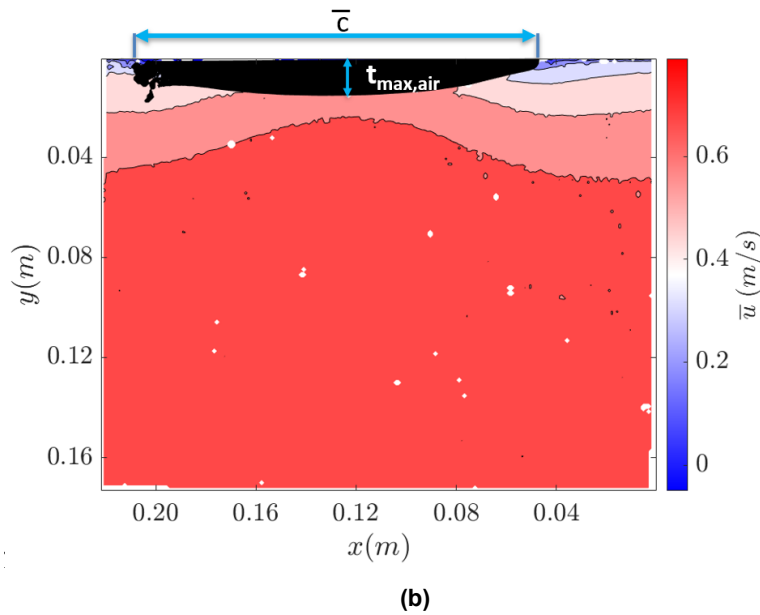
Figure 4.4: (a) Average correlation map over FOV #1 (b) Contour of mean streamwise velocity with the mask of mean air cavity shape (in black) determined using $R_{th} = 0.68$. Also shown is the mean cavity length, $\overline{c}$ and the maximum thickness of the mean air cavity, $t_{max,air}$. Flow is from right to left.

on the windward and leeward side of the air cavity. This flow geometry slightly differs from the solid bump studies of Baskaran et al. (1987) and Webster et al. (1996) in that the incoming TBL in those experienced a short concave region upstream of the bump before the convex region, and the bump was rigid with a well-defined trailing edge compared to the dynamic behaviour of the air cavity here.

The maximum thickness of the mean air cavity $t_{max,air}$, and the mean chord length (or mean cavity length) $\overline{c}$, were found to be 15.6 mm and 160.7 mm in physical units, respectively. The ratio of the initial BL thickness to the maximum air cavity thickness ($\delta/t_{max,air}$) was found to be approximately 6.7. This ratio is considerably higher than in the studies of Baskaran et al. (1987) and Webster et al. (1996), where δ/h was 0.25 and 1.5 respectively (where h is the maximum height of the solid bump), and plays an important role in the development of the TBL. The ratio of the initial BL thickness to the convex radius of curvature in the current study was found to be: $\delta/R \approx 0.329$. This parameter again differs from the studies of Baskaran et al. (1987) and Webster et al. (1996), where this ratio was found to be 0.05 and 0.06 respectively. A discussion on how these parameters play a role in the development of the TBL and affect the comparison of results with the solid bump studies, will follow at the end of the chapter (see section **4.5**).

4.2.2. Variation in maximum air cavity thickness and chord length

As pointed out previously, the chord length $\overline{c}$ and thickness of the air cavity $t_{max,air}$, are important parameters in the study and behaviour of the surrounding flow, as well as for the drag reduction method in general, as it gives an idea of the extent of the non-wetted surface area. Therefore, it is necessary to study how the current detection technique affects the determination of these parameters.

The variance in the thickness of the air cavity along the chord length is shown in figure **4.5a**. At a distance between $0.4\overline{c}$ and $0.6\overline{c}$, where the air cavity achieves its maximum thickness, the variance is at a minimum indicating that the maximum thickness of the air cavity is fairly similar over all instantaneous images acquired. This gives confidence in the estimate of the maximum cavity thickness, important to relevant drag reduction studies. However, with measurements done in a single spanwise plane (as a

result of planar PIV) and the detection method based on correlation values being employed, it is difficult to conclude the location of the spanwise plane at which the maximum cavity thickness is achieved.

There is a higher uncertainty in the estimation of the thickness at the leading and trailing edges of the air cavity, observed by the increase in variance. The rapid rise in variance observed at the trailing edge of the air cavity is essentially due to its dynamic behaviour as pointed out previously. The increase in variance at the leading edge of the cavity is due to the increased spanwise variations of the air-water interface seen at the windward side of the cavity. The air-water interface was observed to be not exactly homogeneous in the spanwise direction due to the unstable nature of the cavity.

(a)
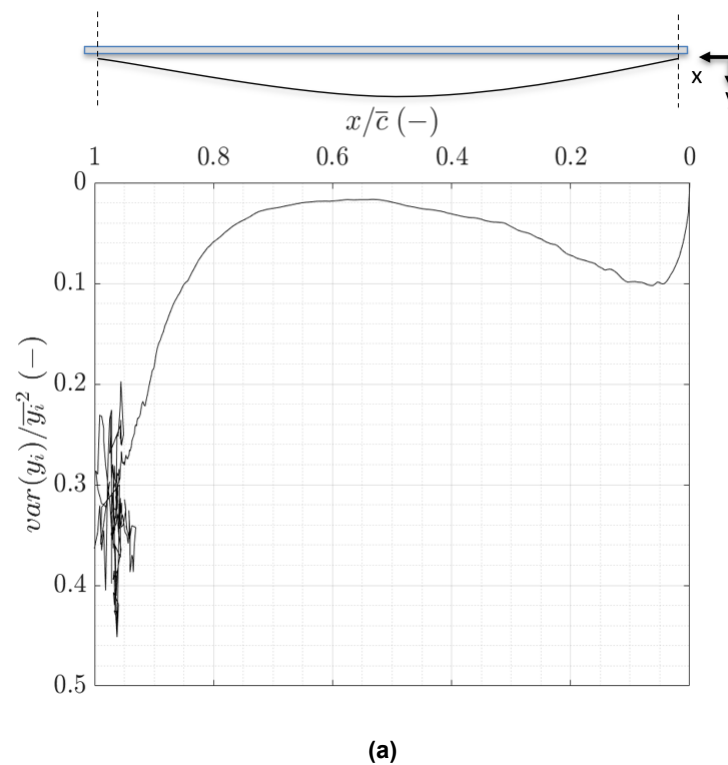
Figure 4.5: See next page for description.

To translate the variance observed in figure **4.5a** into the variation of the thickness with respect to the mean, the deviation in the instantaneous maximum thicknesses of the cavity detected with respect to the maximum thickness of the mean cavity, in % change is shown in figure **4.5b**:

$$dt_{max,i} = \frac{|t_{max,i} - t_{max,air}|}{t_{max,air}} \times 100 \tag{4.1}$$

where $t_{max,i}$ are the instantaneous maximum thicknesses of the cavity detected and $t_{max,air}$ is the maximum thickness of the mean air cavity ($t_{max,air} = 15.6\ mm$). The instantaneous maximum thicknesses detected are seen to vary from about 1 % up to 20 % of the maximum thickness of the mean cavity, with most of the variations observed to occur within 2.5 % of the mean. It is important to point out again that it is difficult to determine the spanwise locations at which the instantaneous maximum thickness was achieved owing to the experimental technique and the detection method employed, in addition to the unstable nature of the air-water interface. Therefore, interpreting the deviation of the instantaneous thicknesses from the mean with respect to a single spanwise plane is not exactly easy.

(b)
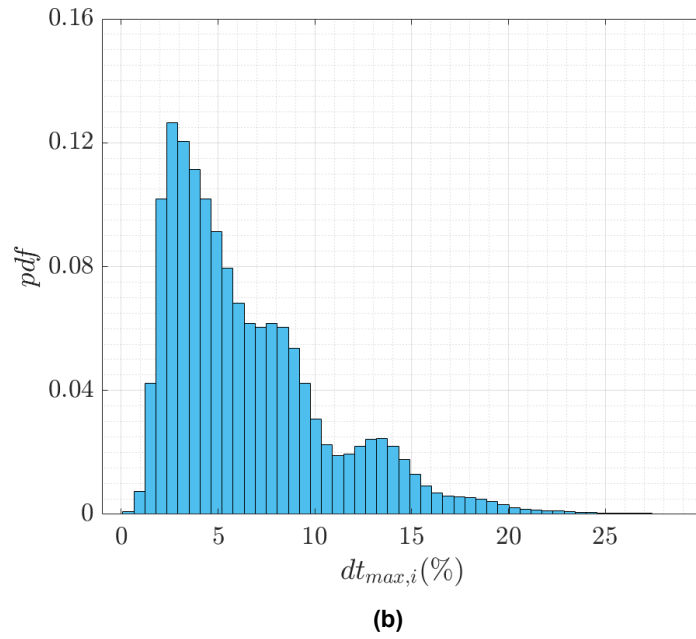
Figure 4.5: (a) Variance in the determination of air cavity thickness along the chord length using $R_{th} = 0.68$. (b) PDF of % deviation in instantaneous maximum thicknesses of the cavity detected with respect to the maximum thickness of the mean cavity ($dt_{max,i}(\%)$) (see equation **4.1**). Bin size used is 0.5 %.
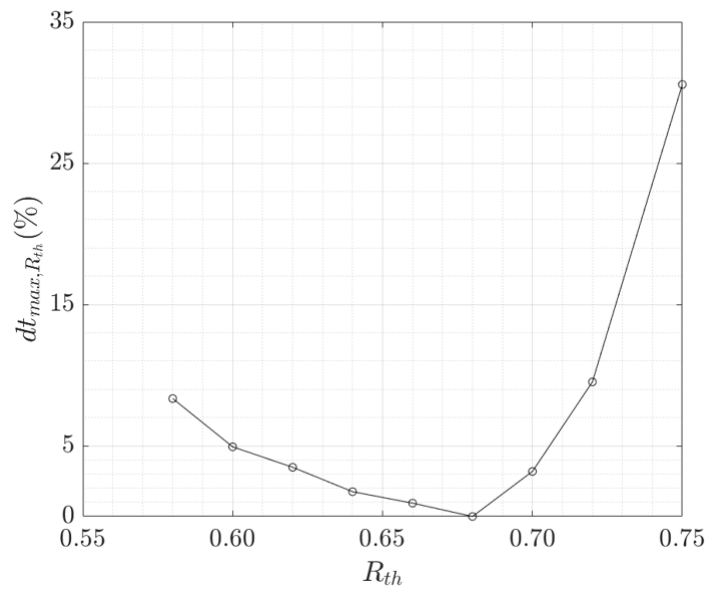
Figure 4.6: Sensitivity of threshold on identifying $t_{max,air}$ through estimation of $dt_{max,R_{th}}(\%)$ (see equation **4.2**).

To study the sensitivity of $t_{max,air}$ on the chosen threshold, its variation (in % change) for various R_{th} values from its reference value obtained at $R_{th} = 0.68$, is estimated (see figure **4.6**) as:

$$dt_{max,R_{th}} = \frac{|t_{max,R_{th}} - t_{max,R_{th}=0.68}|}{t_{max,R_{th}=0.68}} \times 100 \tag{4.2}$$

where $t_{max,R_{th}}$ is the maximum thickness of the mean cavity detected at different R_{th} and $t_{max,R_{th}=0.68}$

is the maximum thickness of the mean cavity detected at $R_{th} = 0.68$. The estimated thickness varies less than 5% for $0.6 < R_{th} < 0.7$, with a gradual increase observed for lower threshold values and a much steeper increase for higher values, indicating the limitations of the chosen detection technique. The steep rise beyond $R_{th} = 0.7$ is due to the sudden jump in correlation values beyond the interface and the inclusion of regions which are part of the surrounding flow. As a result, the maximum thickness of the cavity begins to get overestimated.

(a)

(b)
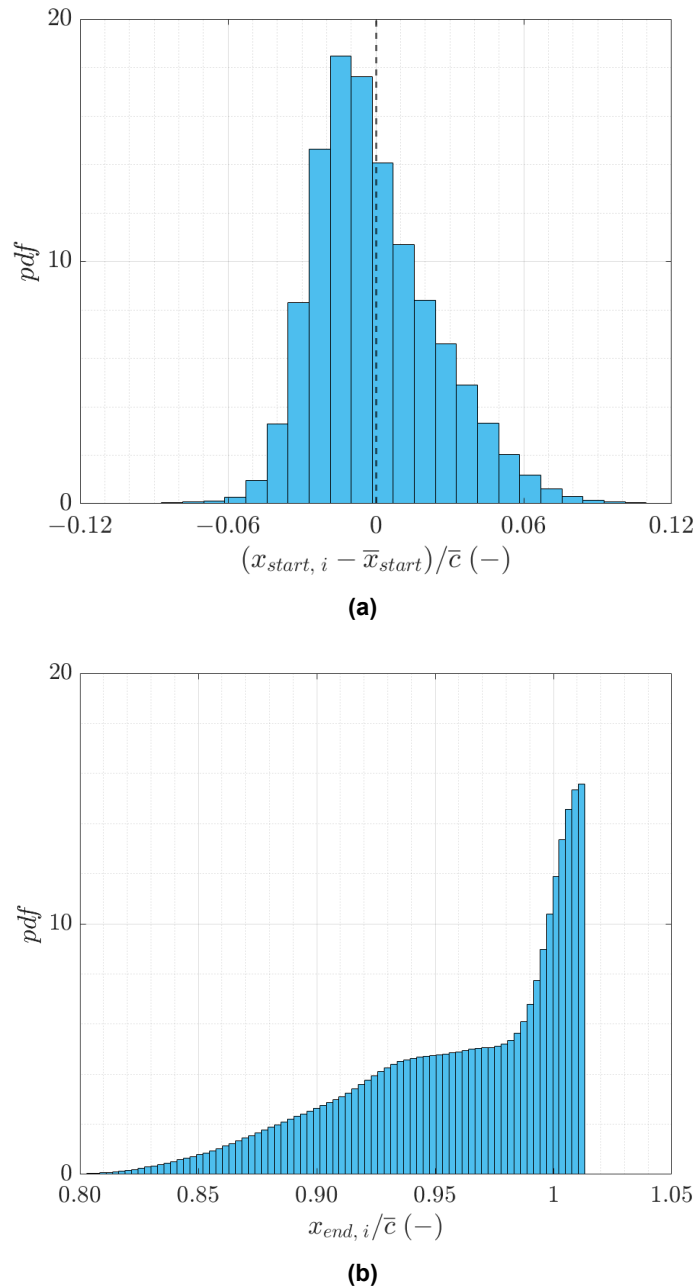
Figure 4.7: (a) PDF of leading edge of the air cavity normalised by mean chord length. Black dashed line represents the mean leading edge of the cavity (b) PDF of trailing edge of air cavity normalised by mean chord length. Bin size used for both is $2\ mm$.

The instantaneous chord lengths identified from each ensemble, depends on the streamwise positioning of the leading edge and trailing edge of the air cavity, which further relies on the detection

technique. A probability density function (PDF) of the instantaneous leading edges of the air cavity normalised by the mean chord length is shown in figure **4.7a**. A variation in the leading edge of the air cavity is observed, with the PDF skewed towards streamwise positions upstream of the mean position. The most probable leading edge position is located at about $0.014\bar{c}$ (or $2.29\ mm$ in physical units) upstream of the mean position. The streamwise positions of the leading edge are observed to vary from $0.05\bar{c}$ upstream of the mean to about $0.07\bar{c}$ downstream of the mean, with the standard deviation of this variation found to be $4.92\ mm$. This deviation is slightly on the higher side considering the fact that the air is injected through a slot of width $4\ mm$. However, when observed visually, the air layer is seen to come out at the same location, and thus any variation greater than the injector slot width should not be expected.

Figure **4.7b** shows a PDF of the instantaneous trailing edges of the air cavity normalised by the mean chord length. A large peak is observed at the tail-end of the PDF, with the most probable ending of the air cavity seen to occur at a streamwise location greater than the mean chord length. This peak at the tail-end of the PDF, might be indicative of the fact that the current FOV might be insufficient to capture the whole air cavity. The standard deviation of this variation was found to be much higher ($7.47\ mm$) than the variation in the leading edge positions of the air cavity, which is a consequence of the dynamic behaviour of this region of the air cavity. However, it should be kept in mind that an accurate estimate of the standard deviation pertaining to this dynamic behaviour is only possible if the whole air cavity is captured. Subsequently, the variations observed in the leading edge and trailing edge positions of the air cavity affect the instantaneous chord lengths detected. When visually observed during experiments, the variation in the leading edge positions of the air cavity was minimal, and the air cavity was seen to end beyond the FOV considered.

In the analysis that follows, the leading edge of the cavity will be considered constant to keep in line with what was observed experimentally, neglecting the variation displayed due to the detection technique. Therefore, the distribution of the normalised cavity lengths (not shown here) will now only contain the variations seen in the trailing edge as seen in figure **4.7b**.

4.2.3. Stations for analysis
In order to study the development of the TBL from the flat surface of the plate to the convex region of the air cavity, different streamwise stations were considered. This promotes ease and brevity for the analysis to follow. The non-dimensional streamwise coordinate $x' = (x - x_o)/\bar{c}$ is used, where x_o is the leading edge of the air cavity, and $\bar{c}$ is the mean cavity or chord length. The forthcoming analysis was also performed using the instantaneous cavity lengths as a normalisation, and did not alter the results presented. As a result, normalisations based on either the mean cavity length or instantaneous cavity lengths could be used, and the mean cavity length is therefore considered in the analysis that follows. An illustration of the flow geometry with the normalised streamwise coordinate system $(x' - y')$ is shown in figure **4.8**.
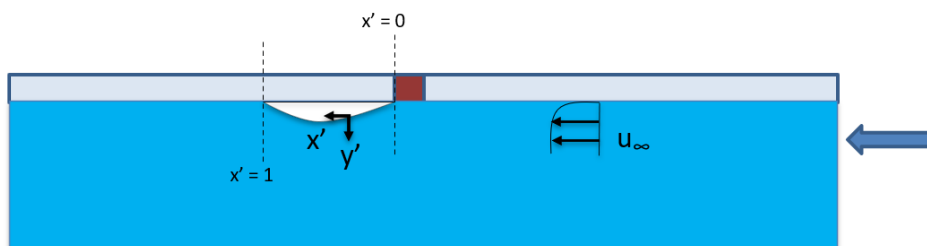
Figure 4.8: Illustration of flow geometry with a non-dimensional streamwise coordinate system $(x' - y')$.

Here, $x' = 0$ and $x' = 1$ are the leading and trailing edges of the mean air cavity respectively.

Further, the y-axis was shifted based on the interface height, and was maintained normal to the flat plate at the interface positions. This concludes the discussion on the detection of the air-water interface. The influence of the air cavity on the development of the TBL is analysed in detail in the sections that follow.

4.3. TBL variation upstream of the injector

As the flow develops from the exit of the contraction, it is expected that the TBL starts feeling the presence of the air cavity at a certain streamwise distance upstream before it encounters the air cavity due to an adverse pressure gradient (APG) (Baskaran et al. (1987); Balin et al. (2021)). To quantify this distance, four stations upstream of the injector were considered as shown in figure **4.9**, with a comparison made between the baseline TBL (no air injection, refer section **4.1**) case and the case when air was being injected.
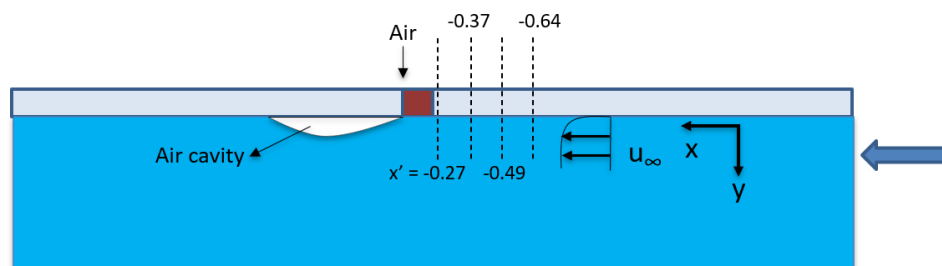
Figure 4.9: Illustration of locations of considered upstream stations. Flow is from right to left.

The mean streamwise velocity profile scaled with the local free-stream velocity and the local boundary layer thickness is shown in figure **4.10a**. The local boundary layer thickness used here was computed based on the composite profile fit. The inner and logarithmic regions exhibit a deviation below the mean velocity profile of the baseline TBL case at the stations $x' = -0.27$, $x' = -0.37$ and $x' = -0.49$. The presence of the air cavity is also seen to cause a slight deviation in the wake region at the most downstream station $x' = -0.27$, although one would not expect a large change in this region considering the scaling parameters used. Moving upstream, the flow is seen to relax to its baseline state in between the stations $x' = -0.49$ and $x' = -0.64$, indicating that the incoming TBL no longer feels the presence of the air cavity beyond this. In physical units, this amounts to $8.5 - 9.5\ cm$ upstream of the injector location. Figure **4.11a** shows the mean streamwise velocity profile scaled in inner units. A noticeable feature observed as the TBL moves downstream is the presence of a rising wake relative to u_τ, which was also observed in the studies by Monty et al. (2011) and Harun et al. (2013) in TBLs subjected to APG, when normalised in inner units. Focusing on the log region, there is a collapse in the outer part of the log-law which starts to slightly deviate (shift downwards) at lower wall-normal distances. A shift of the mean velocity below the log-law for increasing APG was reported by Monty et al. (2011), and in the solid bump studies of Baskaran et al. (1987) and Balin et al. (2021). On the other hand, for TBLs subjected to mild APG, the inner and logarithmic regions were shown to exhibit no deviation from a ZPGTBL (Harun et al. (2013)).

Figure **4.10b** shows the streamwise TI normalised by outer variables. A collapse is observed in the outer region above $y \approx 0.4\delta$. As the TBL moves downstream, the turbulence intensity is seen to amplify below $y \approx 0.4\delta$. As observed in the mean velocity profile, the TBL no longer the effects of the air cavity upstream of the station, $x' = -0.64$.

(a)

(b)
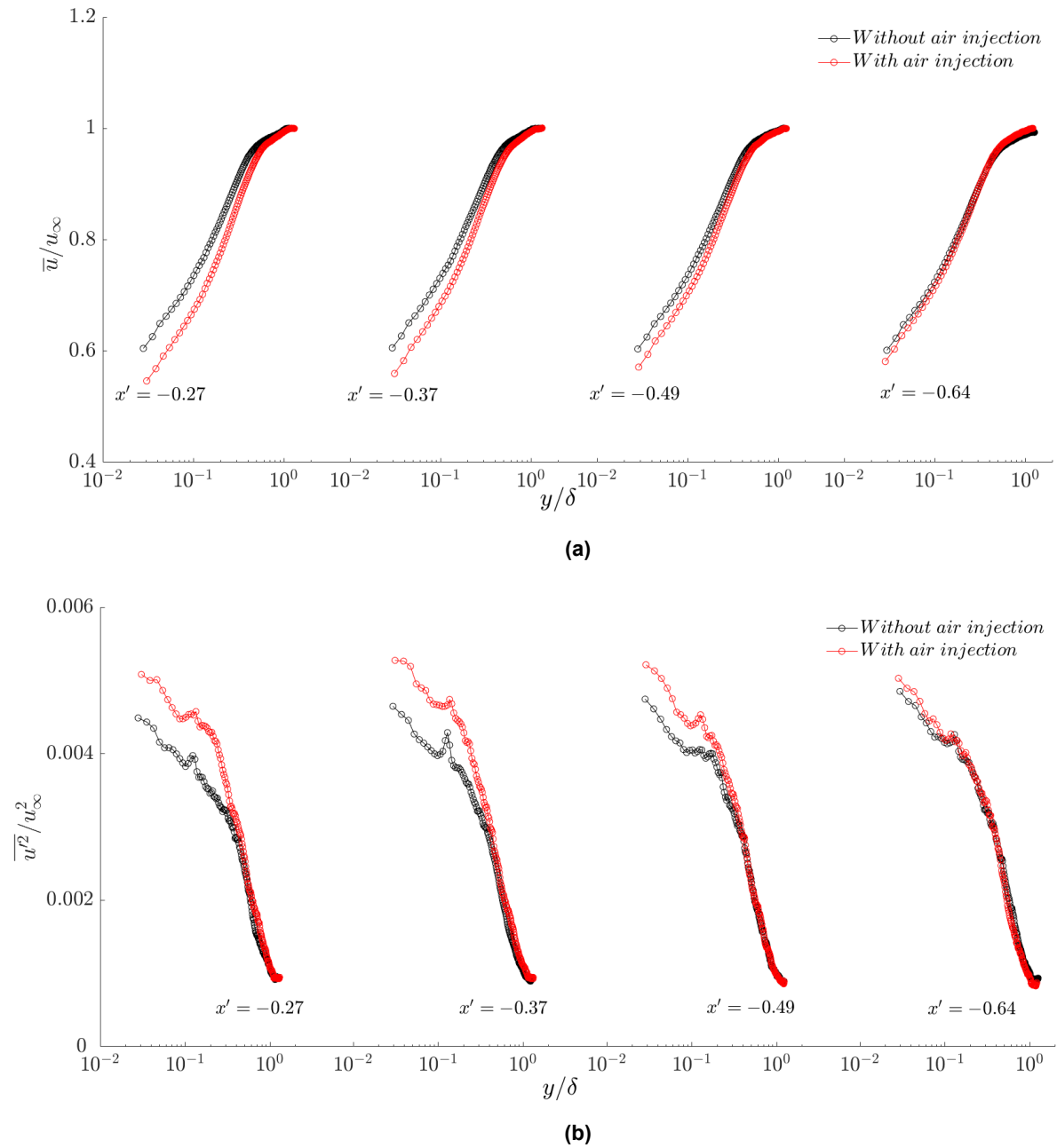
Figure 4.10: Upstream influence of air cavity on the (a) Mean streamwise velocity (b) Streamwise TI. Both the profiles are normalised by outer variables.

To demonstrate that the observed collapse in the outer region is not due to the scaling parameters used, the streamwise TI in inner units is shown in figure **4.11b**. Once again, a clear collapse is observed in the outer region, with the TI in the inner region amplified with increasing downstream distance. Similar behaviours were observed in the wall-normal TI and the RSS, and is not shown here for clarity. Studies have reported increasing TI throughout the TBL when subjected to an APG, with the most increase occurring in the outer region (Monty et al. (2011), Harun et al. (2013)). The differences observed here in terms of the region affected compared to the above studies can be explained as follows: in the current study, the APG is imposed on the incoming TBL as a result of the curvature of the cavity obstructing the flow, while in the aforementioned studies, the APG was applied by adjusting the ceiling of the wind tunnel.

(a)

(b)
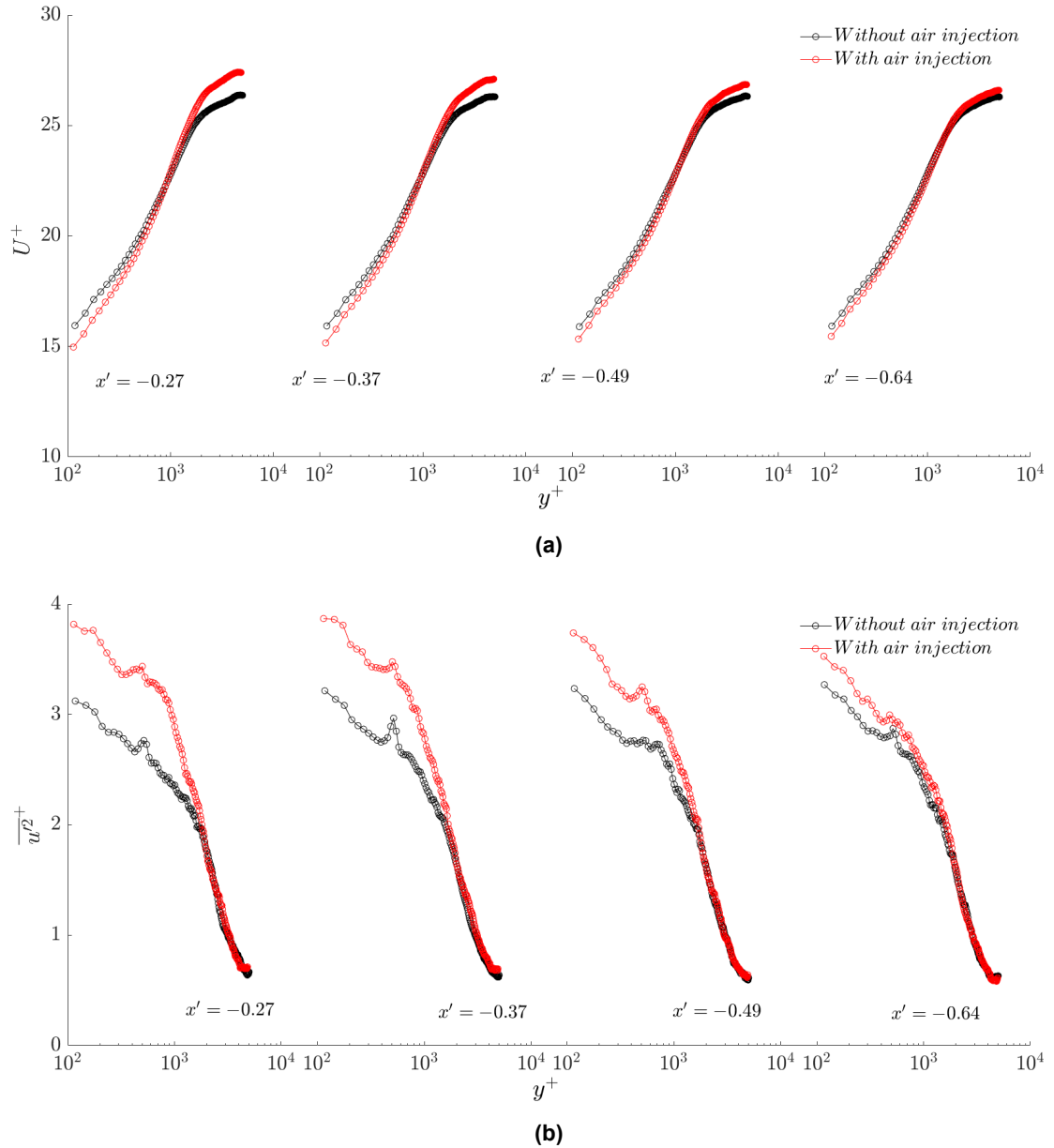
Figure 4.11: Upstream influence of air cavity on the (a) Mean streamwise velocity (b) Streamwise TI. Both the profiles are normalised by inner variables.

4.4. TBL variation downstream of the injector

4.4.1. Boundary layer thickness variation

In the previous section, the "obstruction" by the air cavity was felt by the TBL up to a certain streamwise distance upstream resulting in an APG while the TBL was moving over the flat surface of the plate. Moving downstream, the TBL impinges on the air cavity as it transitions from a flat surface of the plate to the convex region of the cavity. In order to understand the influence of the air cavity on the development of the mean flow downstream, a contour map of the mean streamwise velocity encompassing the whole air cavity is shown in figure **4.12**.
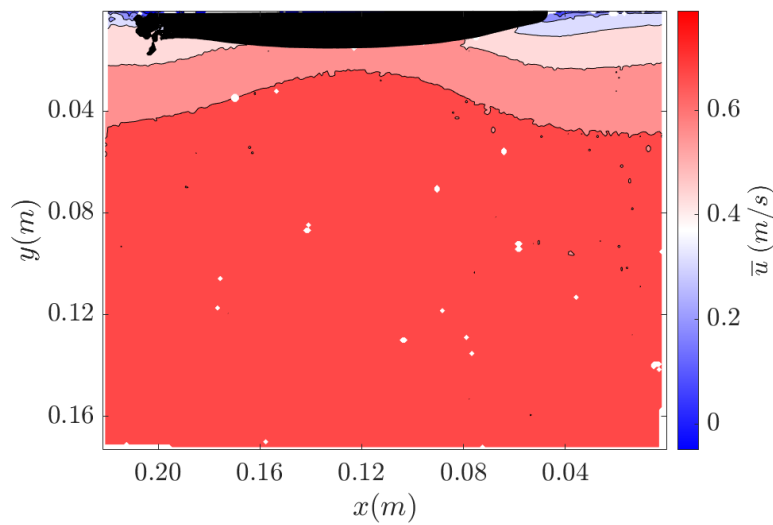
Figure 4.12: Contour map of mean streamwise velocity showing the development of the mean flow underneath the air cavity (shown in black). Flow is from right to left.
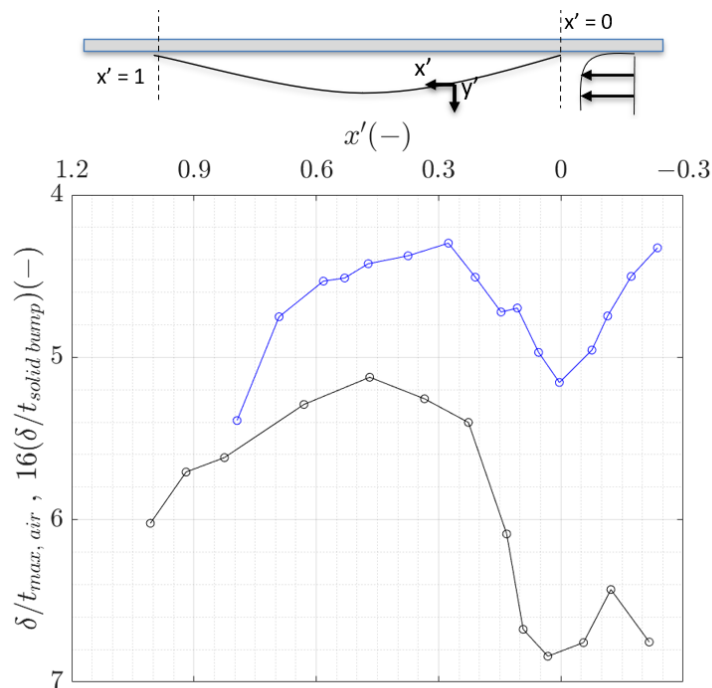
Figure 4.13: Variation of the turbulent boundary layer thickness, δ across the cavity length in the non-dimensional streamwise coordinate system ($x' - y'$). For the current study (in black) the local δ is normalised by the maximum air cavity thickness; also shown is the local TBL thickness normalised by the thickness of the solid bump from the study of Baskaran et al. (1987) (in blue). Flow is from right to left. The TBL thickness is seen to follow the presence of alternating pressure gradients.

At streamwise locations upstream of the air cavity, the TBL was seen to feel an APG mainly affecting

the inner region. As the TBL approaches the leading edge of the air cavity, the contour map reveals a slight bump in the contour lines with higher mean velocities being reached at slightly higher wall-normal locations. This is indicative of an APG acting at this location. The TBL then moves over the convex region where the flow is seen to accelerate reaching higher mean velocities at lower wall-normal locations until approximately the apex of the air cavity, where the acceleration appears to be the maximum. The mean flow then appears to decelerate downstream of the apex. This acceleration followed by deceleration is representative of an alternating streamwise pressure gradient: from an APG at the leading edge of the air cavity to a FPG over the windward side of the air cavity followed by an APG on the leeward side of the air cavity.
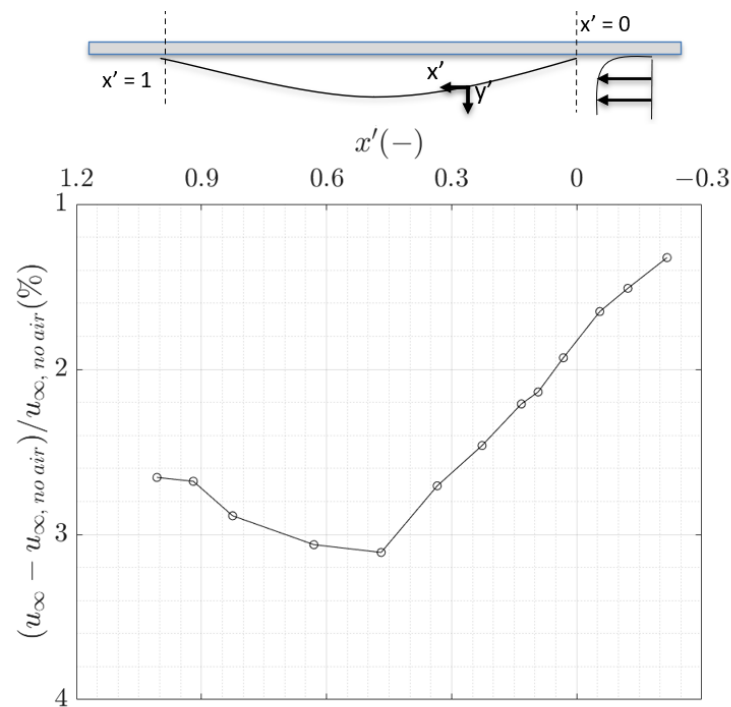
Figure 4.14: Percentage change in local free-stream velocity (u_∞) at different non-dimensional stream-wise locations (x') with respect to the free-stream velocity at the upstream location where the effects of the air cavity were no longer felt ($u_{\infty,no\ air}$). Flow is from right to left.

The presence of alternating streamwise pressure gradients can be further analysed by observing the development of the local TBL thickness (in black) shown in figure **4.13**. The local TBL thickness of the flow over the flat plate in section **4.3**, was estimated using the composite profile fit. However here, the local TBL thickness was estimated by considering the point where the turbulent stresses begin to plateau towards an approximately constant value in the free-stream. An average of the points where the streamwise TI, wall-normal TI and the Reynolds shear stress (RSS) begin to plateau was estimated to be the local δ of the TBL. The estimation of δ using the δ_{99} or the composite profile fit in the region close to the air cavity was difficult and more uncertain owing to the changes in the flow. The study by Vinuesa et al. (2016) discussed the difficulties in the determination of the local free-stream velocity and the boundary layer thickness in pressure gradient TBLs. The fact that the mean velocity is not essentially constant and the gradient du/dy is not exactly zero beyond the boundary layer edge in non-equilibrium TBLs, can make the estimation of δ problematic. Vinuesa et al. (2016) reported the composite profile fit to be not robust and give inconsistent results in the estimation of outer parameters in strong pressure gradient TBLs, and had to resort to a method based on the diagnostic plot (more on diagnostic plot by Alfredsson et al. (2010)) for a consistent estimate of δ.

For comparison, the boundary layer variation over a solid bump observed in the study by Baskaran et al. (1987) is shown (in blue). The variation of the TBL thickness in the current study follows the trend set by the alternating pressure gradients. In the presence of an APG at the leading edge of the air cavity, a small growth in δ is observed between $x' = -0.05$ and $x' = 0.03$, though is not very prominent. The TBL thickness is then seen to reduce as the flow accelerates over the convex curvature (due to a FPG) until just upstream of the apex of the air cavity (around $x' = 0.47$). It is seen to reduce by approximately 24% of its initial thickness. Following the apex, δ is seen to rapidly increase until the most downstream point considered in the analysis. The trend of this variation in δ, is similar to that observed in the study by Baskaran et al. (1987), although the scale difference was large ($\times$ 16) as a consequence of the difference in the ratio $\delta/t_{max,air}$ between the two studies ($\delta/t_{max,air} = 6.7$; $\delta/h = 0.25$, where h is the maximum height of the solid bump). It is important to note here that the TBL did not separate at the leeward side of the cavity which can be explained due to a high $\delta/t_{max,air}$ ratio. On the other hand, separation was observed at the leeward side of the solid bump in the study of Baskaran et al. (1987) where the ratio δ/h was much smaller. Further, of interest is the streamwise position where the TBL thickness achieves its minimum. In the case of the solid bump (Baskaran et al. (1987)), the local δ reached its minimum at a larger upstream distance compared to the current study.

The variation in the local free-stream velocity at different streamwise locations is shown in figure **4.14**. Note that the percentage difference with respect to the free-stream velocity at the upstream location where the effects of the air cavity were no longer felt is considered here. The free-stream velocity is seen to increase and accelerate from the leading edge of the air cavity until a streamwise distance just upstream of the apex. The maximum difference in the free-stream velocity occurs approximately at $x' = 0.47$, where the flow achieves its maximum velocity. At the apex of the air cavity, there is a maximum reduction in flow area, thus enabling the fluid to reach its maximum velocity as a consequence of continuity. The 3.1% change observed in the free-stream velocity at the apex was found to be a fairly good estimate based on the reduction in flow area. Downstream of the apex, the local free-stream velocity decreases which is accompanied by the thickening of the BL (see figure **4.13**), and can be attributed to the presence of an APG.

The behaviour of the above discussed flow parameters shows that the TBL undergoes changes in response to an alternating streamwise pressure gradient imposed by the shape of the air cavity. To gain further insight into how these changes translate into changes observed in the structure of the boundary layer, higher order statistics need to be analysed, and this is the next topic of discussion.

4.4.2. Mean velocity and statistics at Leading edge, Apex and Trailing edge of cavity

The incoming TBL about to impinge the air cavity first experiences a perturbation due to an APG. In the preceding analysis of the TBL upstream of the injector (section **4.3**), the APG was seen to affect mainly the inner region of the BL, while the outer region for the streamwise TI showed similarity when normalised with inner and outer variables. For the rest of the analysis in the current study, the local outer variables will be used for scaling such that the variation in u_∞ and δ are accounted for.

First, we focus on the region around the leading edge of the cavity, which includes the last part of the APG influencing the TBL upstream of the injector (section **4.3**). The mean streamwise velocity profiles and stresses at four non-dimensional locations are shown in figure **4.15**. The maximum variation in the mean velocity profiles (figure **4.15a**) is seen to occur in the inner and logarithmic regions. The station at $x' = -0.05$ shows a velocity deficit mostly in the inner region compared to the station $x' = -0.21$ as a result of the APG. At the beginning of the convex curvature, the flow accelerates due to a switch in the pressure gradient to a favourable one, as observed by the increase in the mean velocities at stations $x' = 0.03$ and $x' = 0.10$. In addition, a slight deviation from the logarithmic behaviour is seen in these stations.

(a)

(b)
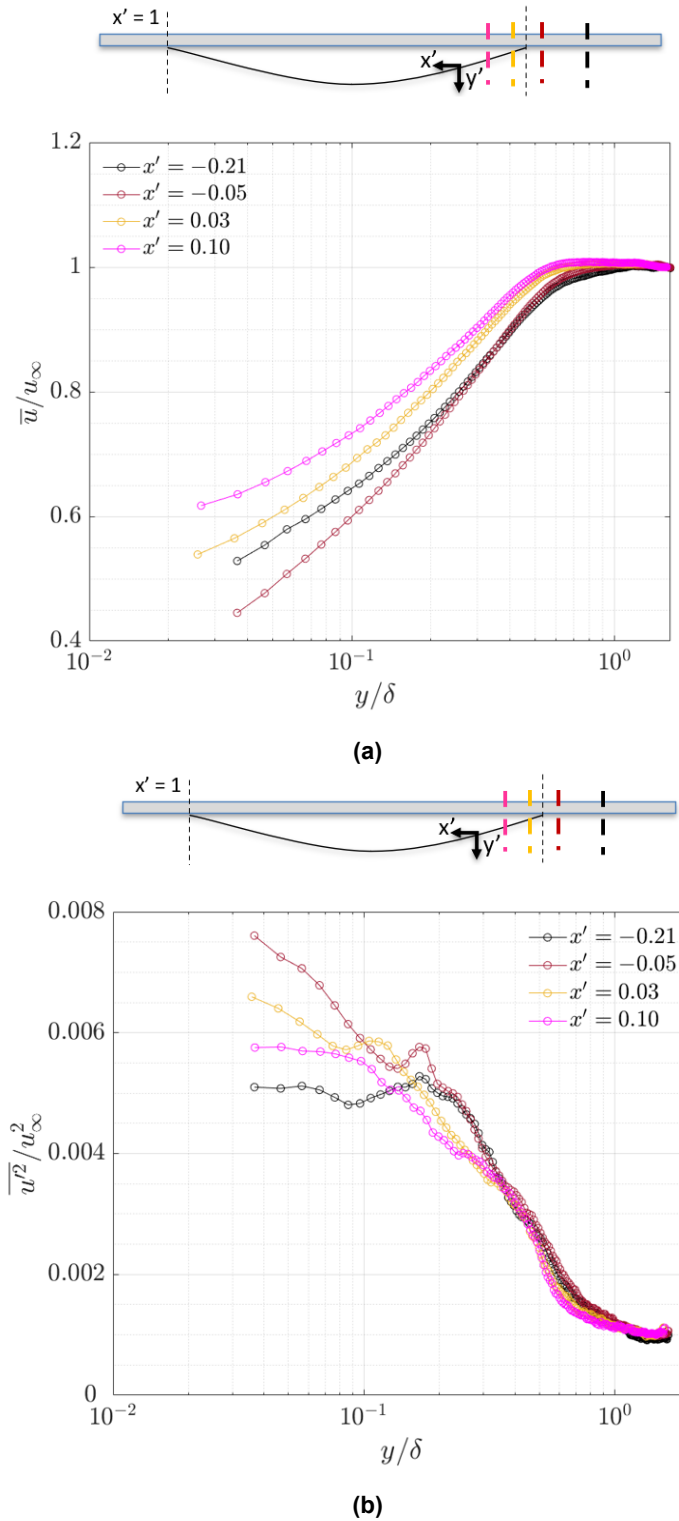
Figure 4.15: See next page for description.

The streamwise and wall-normal TI as well as the Reynolds shear stress (RSS) experience changes due to the pressure gradient variation (see figures **4.15b**, **4.15c** and **4.15d** respectively), with the wall-normal TI and the RSS showing the strongest variation compared to the flat plate case (in black). The variation observed across the four stations in the streamwise TI in the inner region is not so drastic as compared to the wall-normal TI and the RSS. A collapse is seen in the outer region above $y \approx 0.4\delta$
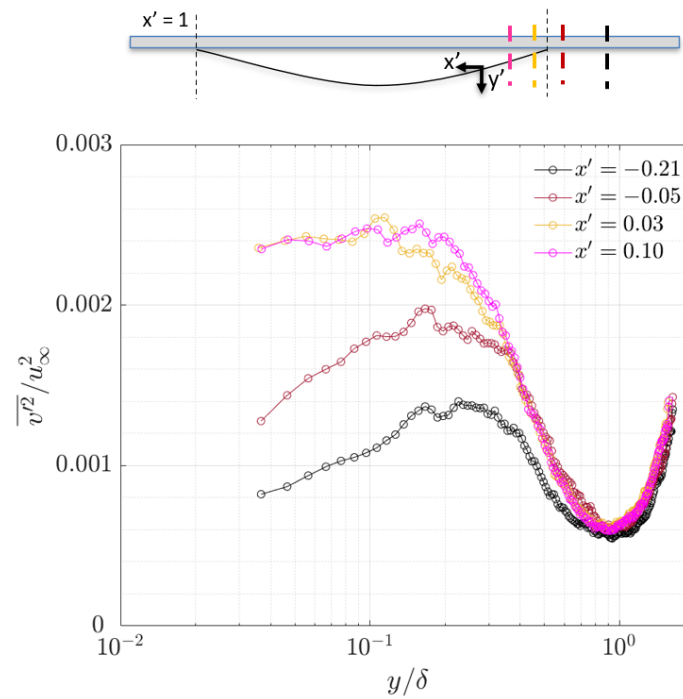
(c)
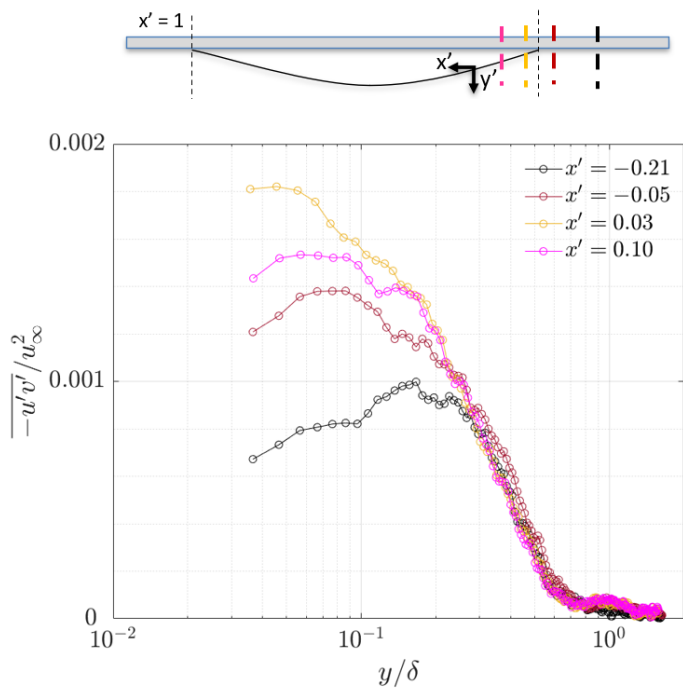
(d)

Figure 4.15: Changes to (a) Mean streamwise velocity (b) Streamwise TI (c) Wall-normal TI (d) Reynolds shear stress around the leading edge of the cavity. All the profiles are normalised by local outer variables. Colours represent different non-dimensional streamwise locations (in $x' - y'$ coordinate system) as shown in an illustration of the air cavity, and in the legend. Flow is from right to left.

for the streamwise TI and RSS. The station at $x' = -0.05$, shows an amplification in the streamwise TI as a result of the APG, which is suppressed as the flow moves downstream due to the stabilising influence of acceleration. On the other hand, the wall-normal TI does not seem to show this expected trend. Instead, the fluctuations at $x' = 0.03$ and $x' = 0.10$ are much higher compared to the station where an APG acts ($x' = -0.05$). Considering that these two locations ($x' = 0.03$ and $x' = 0.10$) are downstream of the injection location, it might be possible that the air injection contributes to this increase in turbulent fluctuations observed. The RSS profile shows a collective picture of the effects seen in the other two components of stress. There is an amplification of shear stress at $x' = -0.05$ due to an APG, followed by a further amplification at $x' = 0.03$ due to air injection and finally a stabilisation of shear stress at $x' = 0.10$ as a result of the FPG. Overall, the effects of the leading edge region of the air cavity on the TBL seem to be contained below $y \approx 0.4\delta$. With similar scaling (using outer variables), Baskaran et al. (1987) reported an increase in stresses throughout the TBL (up to the wake region) at the leading edge of the solid bump which was attributed to streamline curvature caused by the concave region preceding the convex curvature. This possibly indicates the minimal influence of streamline curvature above $y \approx 0.4\delta$ in the current study, with the TBL only being affected up to the lower part of the outer region due to streamwise pressure gradients and air injection.

The APG experienced by the incoming TBL at the beginning of the air cavity causes changes to the TBL structure as seen above with a deviation from the classic logarithmic behaviour and an alteration to the turbulence intensities. Studies have shown a change in scale contributions concurrent with an amplification of TI in boundary layers subjected to APG compared to a ZPGBL (Monty et al. (2011); Harun et al. (2013)). The changes in the TBL seen above (figure **4.15**) is representative of the pressure gradient changing from an APG to a FPG at the windward side of the air cavity. The effect of the FPG will be discussed in more detail in what follows for the region around the apex of the cavity.

The variation of the TBL around the apex and towards the trailing edge of the air cavity, as it moves below it, is now discussed. Mean streamwise velocity and stress component profiles across the streamwise stations considered in this region of the cavity are shown in figure **4.16**. Moving from stations $x' = -0.21$ (black) to $x' = 0.47$ (blue) in the mean velocity profiles (see figure **4.16a**), the flow accelerates on the windward side of the air cavity owing to the FPG originating close to the leading edge as mentioned previously (see figure **4.15**). A systematic deviation from log-law behaviour can be observed especially at the apex of the air cavity ($x' = 0.47$), where the BL thickness was also found to be at its thinnest. This strong deviation from the log-law was also observed by Narasimha et al. (1979) in strongly accelerated flows caused by the stabilising effect of the FPG. They reported the streamwise pressure gradient to mainly influence the inner region, and cause it adopt a quasi-laminar state. The acceleration parameter $K = \frac{\nu}{U_e^2} \frac{dU_e}{dx}$ based on the streamwise gradient of the local external velocity U_e which is typically used to characterise pressure gradient TBLs, was found to be approximately 2.3×10^{-7} at the apex of the air cavity. This value is lower than the observed threshold of $K \approx 3 \times 10^{-6}$ observed in studies which marks the start of the reverse transitional process (turbulent to laminar) (Narasimha et al. (1979)), and therefore we do not expect a relaminarisation to take place here. Moving downstream, an APG begins to act beyond $x' = 0.47$ as seen by the decreasing mean velocity profiles.

Looking at the different stress profiles for this region (see figures **4.16b**, **4.16c** and **4.16d**), similar observations can be made to those seen in the first APG the TBL experiences, around the leading edge of the air cavity. Most of the variations occur in the inner and lower part of the outer region at least for the streamwise TI and the RSS, with the region above $y \approx 0.4\delta$ showing a near collapse under outer-scaling. On the other hand, the variations in the wall-normal TI in the inner and outer regions are much larger especially between the flow at $x' = -0.21$ and the other downstream stations. The streamwise TI displays a smaller jump in TI between stations compared to the other two stresses. Even though the effect of a FPG kicks in before $x' = 0.10$ as seen in the mean velocity profile around the leading edge of the cavity (see figure **4.15a**), the streamwise TI at this station is higher compared to $x' = -0.21$

below $y \approx 0.15\delta$. As expected, an increase in the streamwise TI is observed downstream of the apex due to an APG.

(a)

(b)
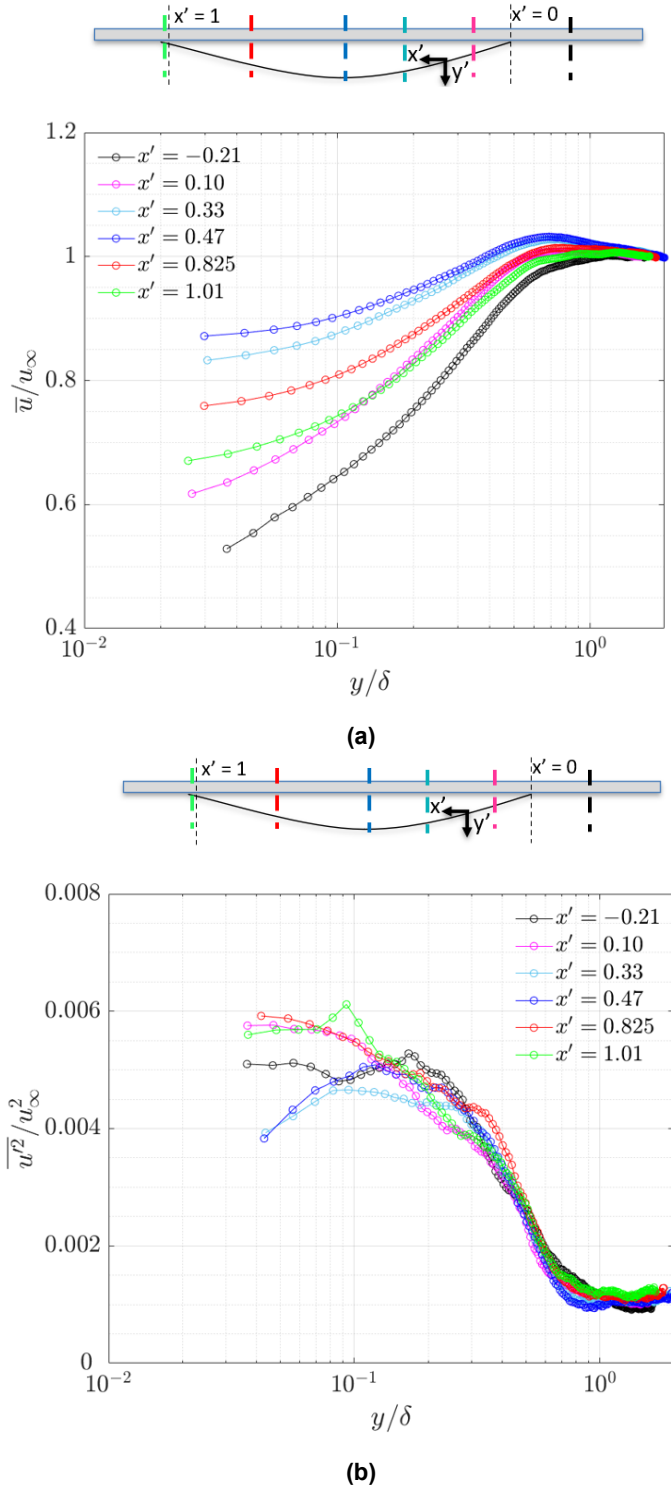
Figure 4.16: See next page for description.

Of interest in the profile of the wall-normal TI is the level of fluctuations at $x' = 0.10$ and $x' = 0.33$ which is comparable to the level at $x' = 0.825$ and $x' = 1.01$ where an APG is present. As the flow transitions from a FPG to an APG across those stations, an increase in TI should be expected as the

(c)

(d)
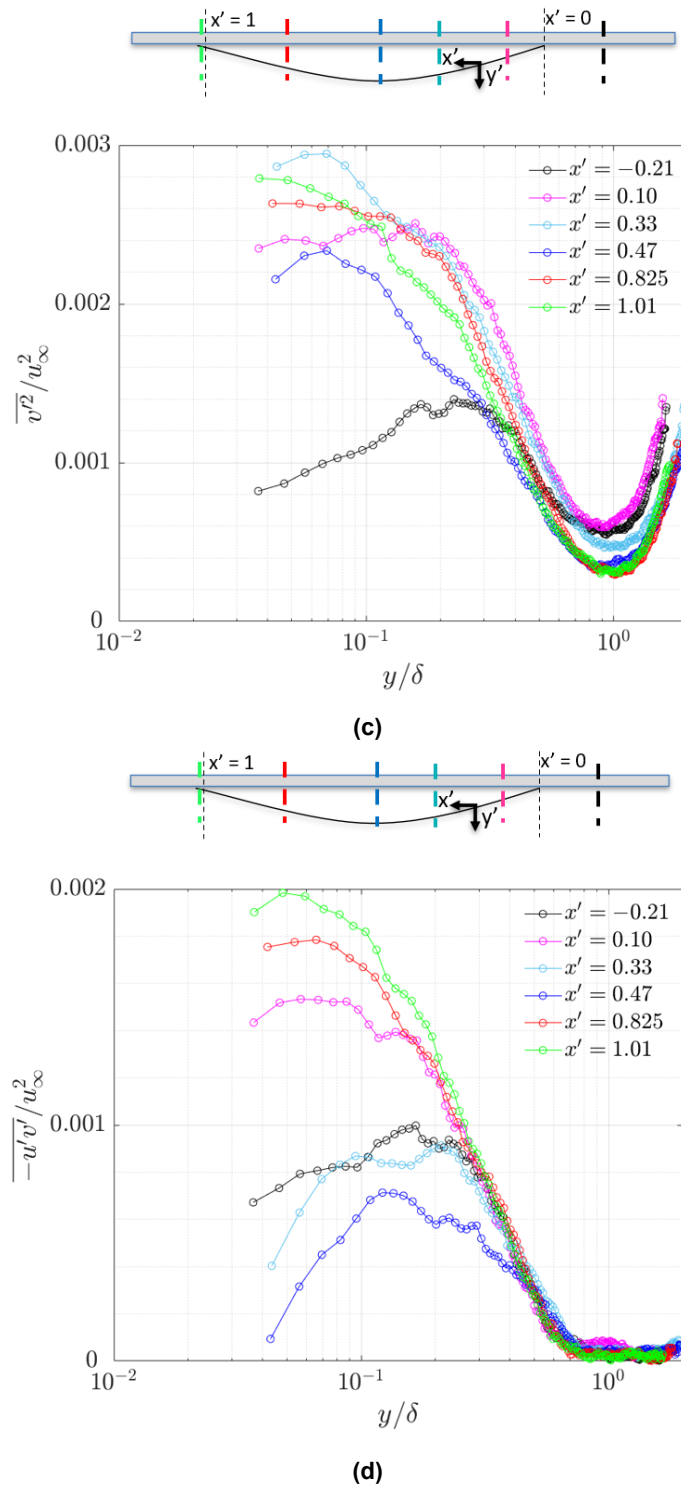
Figure 4.16: Changes to (a) Mean streamwise velocity (b) Streamwise TI (c) Wall-normal TI (d) Reynolds shear stress at the apex and leeward side of the cavity. All the profiles are normalised by local outer variables. Colours represent different non-dimensional streamwise locations (in $x' - y'$ coordinate system) as shown in an illustration of the air cavity, and in the legend. Flow is from right to left.

pressure gradient becomes unfavourable. The relatively similar magnitude of the wall-normal TI in all stations as compared to the flat plate case (shown in black) however, indicates potential dominance of air injection over any pressure gradient effects. A clearer picture on the effects of both the air injection and the alternating pressure gradients can be observed in the RSS profiles. The variation observed downstream of the first station at $x' = -0.21$ can be explained as follows: an increase at $x' = 0.10$ possibly due to air injection, a decrease at $x' = 0.33$ and $x' = 0.47$ due to a FPG and again an increase at $x' = 0.825$ and $x' = 1.01$ due to an APG.

Comparing the above observations with literature, Baskaran et al. (1987) and Webster et al. (1996) in solid bump flows reported knee-points in the stress profiles at locations over the convex curvature. The turbulent stresses below these knee-points grew, and that was attributed to the formation of an internal layer. However, the current stress profiles do not seem to show such behaviour, although the limitations of the current measurement technique (PIV) compared to higher spatial resolution from hot wire measurements in those studies, might have also played a role in that. With similar scaling, Baskaran et al. (1987) reported a gradual decrease in stresses in the outer region due to streamline curvature. This was not observed in the study by Webster et al. (1996) where only mild variations were seen in the outer region, an effect attributed to the minimal influence of streamline curvature by the author. The similarity observed above the lower part of the outer region ($y \approx 0.4\delta$) of the flow in the current study might thus indicate that the effect of streamline curvature is not that important compared to those of the streamwise pressure gradients and the air injection, the latter of which was absent in all solid bump studies.

4.4.3. Quadrant events

Looking into a more fundamental aspect, quadrant analysis gives information on the RSS producing events and hence the TKE production, as well as on the momentum transport in a TBL. Further, it can help shed some light into the turbulent behaviour in the inner and outer regions.

(a)
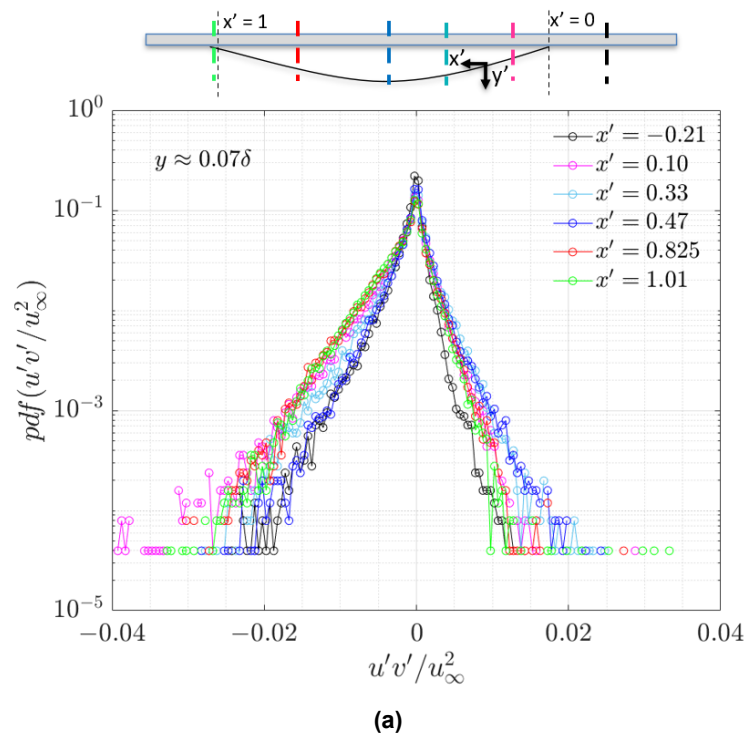
Figure 4.17: See next page for description.

The ensemble-averaged RSS discussed in the previous subsection (refer section **4.4.2**), was able

(b)
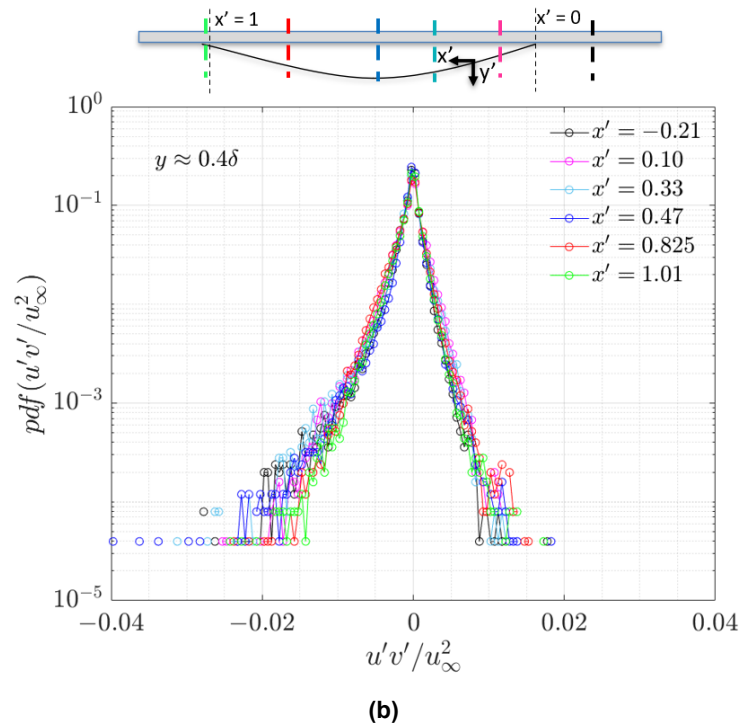
Figure 4.17: Comparisons of PDF of the normalised instantaneous shear stress across different streamwise locations in the $x' - y'$ coordinate system at two wall-normal locations: (a) $y \approx 0.07\delta$ (b) $y \approx 0.4\delta$. Colours indicate different streamwise locations with locations shown in the legend.

to capture the influence of the streamwise pressure gradient imposed by the curvature of the air cavity on the flow, as well as the influence of air injection across different streamwise locations. It is then interesting to analyse how the RSS production events change in the streamwise direction as a consequence of different influences on the flow.

Figure **4.17** shows a PDF of the instantaneous shear stress normalised by the local free-stream velocity u_∞ across different stations considered at two wall-normal locations: $y \approx 0.07\delta$ (inner region) and $y \approx 0.4\delta$ (outer region). There are two notable features which are readily observable: First, both PDFs are skewed towards the negative side. Second, the variation across stations for the shear stress events is much larger in the inner region. The skewed behaviour towards the negative side is expected as $Q2$ (ejections: $u < 0$ and $v > 0$) and $Q4$ (sweeps: $u > 0$ and $v < 0$) events are the dominant contributors to RSS in a TBL. On the other hand, $Q1$ (outward interactions: $u > 0$ and $v > 0$) and $Q3$ (inward interactions: $u < 0$ and $v < 0$) events are less strong. An increase in both the negative and positive contributions to instantaneous RSS events can be observed with downstream distance at $y \approx 0.07\delta$. In addition, contributions from the positive and negative events vary across different stations, hinting at a possible influence of both the streamwise pressure gradients and the air injection. On the other hand, the PDF in the outer region at $y \approx 0.4\delta$, shows much less variation in the contributions across different stations. This is expected considering the observed collapse in the outer region across all the stations in the ensemble-averaged RSS (see figure **4.16d**).

To get more insight into the change in quadrant events, joint PDFs of the quadrant events across the different stations together with those of the baseline TBL (at $x' = -0.64$) are shown below. The same wall-normal locations were considered: $y \approx 0.07\delta$ (inner region) and $y \approx 0.4\delta$ (outer region). As expected, ejections and sweeps are the major contributors to the RSS production in the inner and outer regions as was observed in figure **4.17**.
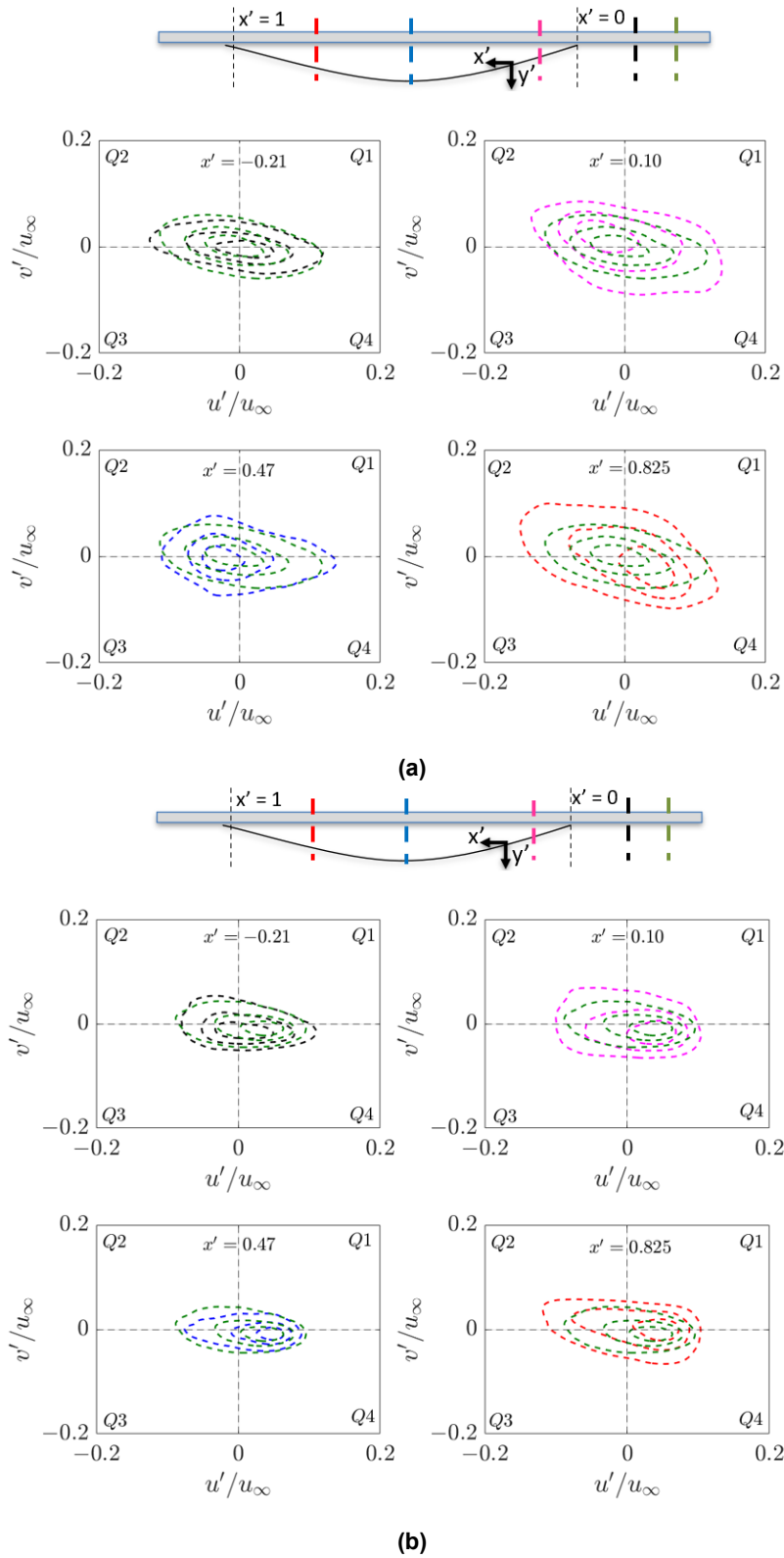
Figure 4.18: Comparisons of joint PDF of the normalised instantaneous streamwise and wall-normal fluctuations across different streamwise locations in the $x' - y'$ coordinate system at two wall-normal locations: (a) $y \approx 0.07\delta$ (b) $y \approx 0.4\delta$. Contour lines represent 20%, 50% and 80% of the maximum probability level. Also shown in dark green is a joint PDF of the instantaneous streamwise and wall-normal fluctuations at $x' = -0.64$ where the effect of the air cavity was not felt by the TBL. Colours indicate different streamwise locations (shown in the inset) as shown in an illustration of the air cavity, with the flow being from right to left.

An interesting feature observed at $x' = -0.47$ in the inner and outer regions, is the lower tilt of the PDF compared to the baseline case, which might indicate a decrease in the turbulent activity as a result of the stabilising effect of the acceleration at that location.

In the inner region, the biggest change in contributions is seen to occur at $x' = 0.10$ and $x' = 0.825$, with an overall increase in all quadrant events compared to the baseline case. Further, the joint PDF appears to be much more elliptical, with the major axis tilted towards the second and fourth quadrants, indicating increased contributions of ejections and sweeps at $x' = 0.10$ and $x' = 0.825$. An interesting feature to note is that the shape of the joint PDF at $x' = 0.825$ looks like a mirror opposite to the one at $x' = 0.10$. Only mild variations in the quadrant contributions can be observed at $x' = -0.21$ and $x' = 0.47$ with respect to the baseline case, with a noticeable increase in inward interactions ($Q3$) seen at $x' = 0.47$.

Focusing on the outer region, the joint PDF is much more circular denoting increasing contributions from $Q1$ and $Q3$. Compared to the inner region, there is much less distinction in quadrant contributions in the outer region between the baseline case and the downstream locations. Similar to the inner region, an overall increase in all quadrant events compared to the baseline case can be observed at $x' = 0.10$ and $x' = 0.825$.

The above plots show that there is an influence of streamwise pressure gradients and air injection on the momentum transport in the TBL developing below the air cavity, which is mostly noticeable in the inner region. The differences seen in the quadrant contributions compared to the baseline case indicates a possible change to the turbulent coherent structuring. However, it is important to note that further analysis is needed to decouple the influence of different factors present in the flow on quadrant events, possibly by breaking them down into individual fractional contributions towards the total RSS produced, but this is outside the scope of the current work.

4.5. Discussion

Results in the previous sections have provided insight into the behaviour of a liquid TBL developing on a flat plate and encountering an air cavity. The air cavity detected in the current study differs from solid bump studies in literature in that first, the boundary condition is changed from a no-slip to a slip boundary condition. Secondly, the bump in the current study is unstable and dynamic, and as a consequence the bump thickness and cavity length are essentially not constant. The detection method seemed to give a good estimate for the maximum thickness, important to relevant drag reduction studies. On the other hand, the detection technique was less successful in accurately capturing the leading edge location of the air cavity, and even less so in capturing the trailing edge, due to its dynamic nature and the smaller than needed FOV. Despite this, all results presented were unaltered when the instantaneous air cavity characteristics were used to normalise the streamwise stations, indicating that the above changes did not significantly affect the analysis here. Finally, it should be noted that all the results refer to a single spanwise plane (since planar PIV was used), and along with spanwise variations of the interface and the detection method being employed, contributes to the uncertainty in the detection of the air-water interface.

No separation was observed in the region downstream of the apex which can be attributed to the high $\delta/t_{max,air}$ ratio of 6.7. The TBL was found to separate in the study of solid bumps by Baskaran et al. ([1987](#)) where the bump thickness was much higher than the BL thickness ($\delta/h = 0.25$). Also, incipient separation was observed in the study of flow over a Gaussian-shaped bump by Balin et al. ([2021](#)) where δ/h was 0.125. The study of an air layer based on a cavitator (backward facing step) based air injection by Zverkhovskyi ([2014](#)), was able to capture the interdependence between the air cavity stability and the $\delta/t_{max,air}$ ratio. For a ratio of $\delta/t_{max,air}$ slightly smaller than 1, he reported the

air cavity to be more stable compared to higher values of the ratio $\delta/t_{max,air}$. It is important to keep in mind that the presence of a cavitator plays an important role in the dynamic interdependence between the air cavity and free-stream conditions observed. On the other hand, the trend observed in the study by Zverkhovskyi (2014) is not expected to be replicated in the current study due to a different method of air injection, and therefore a direct comparison is not feasible.

Another important parameter known as the "curvature parameter" δ/R over the convex region, was found to be 0.329 in the current study. Studies have shown that BL flows over curvature can cause instabilities such as the formation of Görtler vortices (for example a review by Saric (1994)). This instability is caused when the radius of curvature is comparable to the BL thickness. This is not the case in the current situation where the radius of curvature is considerably higher than the BL thickness ($\delta/R \approx 0.329$). In addition, Görtler vortices are observed to form mostly in BL flows over concave curvatures, which is absent in the current flow geometry. Therefore, these vortices are not expected to be formed in the current flow.

Results from the region upstream of the air cavity showed that the TBL was able to feel its influence up to $8.5 - 9.5\ cm$ upstream. The TI and the shear stress normalised in inner and outer coordinates were found to be mostly affected in the inner region seen by an amplification of the TI. An APG imposed by the leading edge of the air cavity was seen to affect the incoming TBL. Studies on TBL subjected to APG (Monty et al. (2011); Harun et al. (2013)) reported an increase in TI not just restricted to the inner region, but throughout the BL when normalised in inner units. In the studies of Monty et al. (2011) and Harun et al. (2013), the maximum increase was found to be in the outer region, as a result of increased contributions from large-scale structures. The difference in the affected region compared to literature, may be attributed to the difference in flow development as the above two studies employed a variable height wind tunnel to impose the APG. On the other hand, in the current study the pressure gradients were imposed as a result of curvature of the air cavity with a non-varying water tunnel height. In general, streamwise pressure gradients can be imposed in multiple ways, for example by using a adjustable height tunnel, introducing curvatures or even through ramps.

Below the air cavity, the TBL experienced perturbations of alternating streamwise pressure gradients, namely: APG at the leading edge of the cavity, FPG at the windward side of the cavity and APG at the leeward side of the cavity. Just upstream of the apex of the air cavity, the flow seemed to achieve its maximum acceleration seen by a minimum in the BL thickness (see figure **4.13**). The effect of this acceleration at $x' = 0.47$, was also observed by a suppression in turbulent fluctuations (see figure **4.16d**). The acceleration parameter $K = \frac{\nu}{U_e^2}\frac{dU_e}{dx}$, was well below the observed threshold of 3×10^{-6} needed for relaminarisation (Narasimha et al. (1979)). The strength of different pressure gradients through the acceleration parameter was difficult to extract owing to the low spatial resolution and the gradient dependency of the parameter. In addition, there is ongoing debate in the scientific community as to whether the acceleration parameter is the right quantity to study the physics of TBLs subjected to pressure gradients, as it does not give much insight into the the near-wall behaviour.

The inner region and the lower part of the outer region of the TBL below $y \approx 0.4\delta$ were the most affected as observed in the streamwise TI and the shear stress profiles (see figures **4.15** and **4.16**). The wall-normal TI did not display the expected trend based on the influence of the alternating streamwise pressure gradients. Instead, the vertical momentum introduced by the air injection seemed to dominate the profile of the wall-normal TI overshadowing any potential pressure gradient effects. The effects of air injection was seen to be felt in the inner and outer regions of the TBL, where no collapse was observed across different stations in the wall-normal TI profile. On the other hand, the streamwise TI and the Reynolds shear stress profiles displayed a combination of the air injection and pressure gradient effects, with the air injection effect more prominent on the windward side of the cavity.

The current study involves a combination of multiple perturbations to the flow, namely pressure gradients, air injection, streamline curvature and a slip condition. The number of parameters at play here renders the current flow more complex than the solid bump studies of Baskaran et al. (1987), Webster et al. (1996) and Balin et al. (2021), where streamwise pressure gradients and streamline curvature were the only ingredients of the flow. The aim of the current study is to make an attempt in identifying where the above perturbations/effects are more prominent, but a complete separation is beyond the scope of this work.

The effect of streamwise pressure gradients are known to first perturb the inner region and then propagate to the outer region in the form of internal layers (Smits (1985)). Internal layers were observed in the stress profiles in the solid bump studies of Baskaran et al. (1987), Webster et al. (1996) and Balin et al. (2021). Baskaran et al. (1987) attributed the formation of an internal layer as a result of change in streamline curvature (from a concave to a convex region). However, in the current study, there was no indication in the stress profiles of the existence of an internal layer, even though there was a change in boundary condition from a no-slip at the surface of the plate to a slip at the air-water interface, and the presence of streamline curvature. It is tempting to attribute the absence of an internal layer either due to a slip condition at the air-water interface, or the perturbation present being insufficient to trigger one. However, owing to the low resolution of the PIV technique and the uncertainty associated with the position of the air-water interface, it is not possible to draw a definite conclusion on this issue.

Minimal variations were seen above the lower part of the outer region (above $y \approx 0.4\delta$) in the stress profiles, indicating that the effect of streamline curvature might not be that important. A gradual decrease in stresses over the convex curvature was observed by Baskaran et al. (1987) when normalised by outer variables, and was attributed to the influence of streamline curvature. So et al. (1975) also reported the effect of streamline curvatures being most prominent in the outer region. Hence, it is possible that the streamwise pressure gradients and air injection are the dominating aspects of this flow. An additional complexity of the effect of slip condition was not readily observable in any of the profiles discussed. Therefore, it is difficult to rule out the influence of slip, and further research may be necessary to isolate the different ingredients of this flow.

The increased influence of the air cavity on the inner region of the TBL compared to the outer region was also supported by the change in quadrant contributions. An increase in overall contributions particularly in the ejections and sweeps was observed at $x' = 0.10$ and $x' = 0.825$ in the inner region of the TBL (see figure **4.18a**). A distinct feature observed here was the mirrored behaviour of both these stations. In TBL subjected to APG, $Q4$ events ($u > 0$ and $v < 0$) were found to dominate over $Q2$ events ($u < 0$ and $v > 0$) in the inner region compared to ZPGBL, where the situation is reversed (Nagano et al. (1998); Tsikata et al. (2013)). Assuming such dominance in an APG (at $x' = 0.825$) and a further increase in outward v' fluctuations because of the air injection (at $x' = 0.10$), could potentially explain the mirrored behaviour seen at these two locations to a certain extent. However, further research is necessary to validate this argument, for instance by breaking the total RSS down into fractional contributions from each quadrant, but is beyond the scope of this study. Finally, the difference seen in the joint distribution of the quadrant events (see figure **4.18**) compared to the baseline case, hints at an alteration to the well-known coherent structuring of a TBL.

<div style="text-align: right; font-size: 3em;">5</div>

Conclusions and Recommendations

This chapter discusses the key takeaways from the current study along with recommendations for improvement of the study and areas for future work.

5.1. Conclusions

The current experimental study analyses the influence of an air cavity on an incoming turbulent boundary layer using using planar PIV measurements. It aims to give insight and build upon the physics of the flow encountered in the application of air layer drag reduction. The flow development below the air cavity in the present study has similarities in flow geometry to the flow over solid bumps (Baskaran et al. (1987); Webster et al. (1996)) in literature. The shape of the bump such as its curvature dictates how the surrounding flow behaves. Unlike solid bumps, where the maximum thickness and the chord length of the bump are constant, the air cavity was seen to have a dynamic and unstable air-water interface with varying chord lengths. A detection technique based on correlation values was used to identify the air-water interface, and obtain an approximate shape of the air cavity. Estimates of maximum thickness of air cavity and its chord length, are important parameters in this method of drag reduction, and in particular understanding the efficiency of its operation. The maximum thickness of the air cavity was approximately located at the apex of the cavity and its value was found to be sufficiently accurate marked by a low variance of the cavity thickness estimate at that location. As a result of the detection technique, the deviation observed at the leading edge position of the air cavity was higher than expected. The field of view currently used to capture the air cavity, was found to be insufficient to capture the whole air cavity especially given the observed dynamic behaviour of its trailing edge.

The incoming turbulent boundary layer was found to feel the effects of the air cavity up to $8.5 - 9.5\ cm$ upstream as a result of an adverse pressure gradient. Alternating streamwise pressure gradients, from an adverse pressure gradient to a favourable pressure gradient and back to an adverse pressure gradient imposed by the curvature of the air cavity, was seen to influence the boundary layer development. No separation was observed on the leeward side of the air cavity which was attributed to a high $\delta/t_{max,air}$ ratio. The flow was seen to achieve its maximum acceleration a little upstream of the apex of the air cavity as observed by a minimum in the boundary layer thickness; however, the acceleration parameter K was found to be lower than the relaminarisation threshold reported in literature (Narasimha et al. (1979)).

Statistics such as the mean velocity profile and stresses, displayed the effects of alternating streamwise pressure gradients and air injection on the turbulent boundary layer, with the inner and lower part of the outer regions observed to be the most effected. Effects of streamline curvature were found to

be not very important. On the other hand, it was difficult to isolate the effect of slip condition, and further research is necessary to get a clearer picture. The presence of an internal layer in the stress profiles was not readily observable, contrary to studies where perturbations to the turbulent boundary layer in the form of sudden change in boundary conditions, triggered an internal layer (Baskaran et al. (1987); Webster et al. (1996); Balin et al. (2021)). Further, changes in the quadrant distributions in the production of Reynolds shear stress compared to a baseline case were observed, possibly indicating a change in the coherent structuring of the turbulent boundary layer. In light of this, further research could be done to investigate the spatial scales involved in the structuring of the turbulent boundary layer under the influence of the cavity. Taking a step further, the air-water interface could also be measured in more detail to determine whether any correlation exists between the scales observed at the interface and in the turbulent boundary layer.

To sum up, in the current study, the formation of an air cavity and its shape depends on the free-stream conditions, and consequently the shape of the air cavity formed dictates how the surrounding flow behaves below it, thus forming a complex coupled system. However, based on a different working principle of air injection (using a cavitator), the study by Zverkhovskyi (2014) highlighted a link between the free-stream conditions and the formation and stability of an air cavity, but the physics of this interdependence were not touched upon. It is expected that the boundary layer development below the air cavity would play an important role in this interdependence. Therefore, conclusions drawn from the current study of a TBL flow below an air cavity, could be useful in providing some insight into understanding this complex flow.

5.2. Recommendations

This section outlines some suggestions on improving the current study and possible ideas for future work. A different technique of detecting the air-water interface may be required, as the current detection technique is dependent on the PIV image quality and may not always work for different datasets leading to unreliable results. PLIF as an interface profiling technique employing an additional profiling camera, might be an option for interface detection, provided the experimental setup permits its execution. The whole air cavity could not be captured with the current FOV, therefore a larger FOV without compromising on the spatial resolution is necessary. In addition, it would be interesting to have a downstream FOV beyond the air cavity to study at what distance the TBL recovers to its baseline state, and no longer remembers its perturbation history. Time-resolved PIV measurements could provide useful insight compared to snapshot PIV data in understanding the dynamic behaviour of the air cavity and its relation to the instantaneous flow organisation.

The variation in the strength of alternating streamwise pressure gradients could not be captured owing to the absence of pressure data and the difficulties in employing the acceleration parameter. Improving the spatial resolution, would possibly help capture the subtle variations in the acceleration parameter to possibly comment on the strength of pressure gradients. On the other hand, the Clauser parameter $\beta = \frac{\delta^*}{\tau_w}\frac{dP}{dx}$, would be a more accurate quantity in detecting the strength of pressure gradients compared to the acceleration parameter, due to its inability to capture the near-wall behaviour. With advancements in analysis of PIV datasets, pressure field estimates are now possible using snapshot PIV data, and are more advantageous over point-wise measurements and could thus provide estimates of the Clauser parameter. The coupling between the air cavity and free-stream conditions, makes it difficult to study the influence of the air cavity (in the current study) on different boundary layer thicknesses. An interesting area of research would be to study the flow over a solid bump with the same configuration of the detected air cavity and free-stream conditions, and identify similarities and differences to the current conclusions. It would give some insight into the influence of a slip boundary condition on the development of the TBL. However, to isolate the multiple ingredients of this flow and study their possible interaction, further investigation for example as in the study of Baskaran et al. (1991) is nec-

essary. Finally, with higher spatial resolutions, it would be interesting to know if any changes occur in the coherent structuring of the TBL under the influence of the air cavity, and if it does, the spatial scales associated with it using velocity correlations.

Bibliography

Adrian, R. J. (2007). Hairpin vortex organization in wall turbulence. *Phys. Fluids*, *19-041301*, 1–16.

Adrian, R. J., Meinhart, C. D., & Tomkins, C. D. (2000). Vortex organization in the outer region of the turbulent boundary layer. *Journal of Fluid Mechanics*, *422*, 1–54.

Adrian, R. J., & Westerweel, J. (2011). *Particle image velocimetry* (First). Cambridge University Press.

Alfredsson, P. H., & Örlü, R. (2010). The diagnostic plot - a litmus test for wall bounded turbulence data. *European Journal of Mechanics B/Fluids*, *29*, 403–406.

André, M. A., & Bardet, P. M. (2015). Experimental study of shear layer instability below a free surface. *Phys. Fluids*, *27, 112103*, 1–13.

André, M. A., & Bardet, P. M. (2017). Free surface over a horizontal shear layer: Vorticity generation and air entrainment mechanisms. *Journal of Fluid Mechanics*, *813*, 1007–1044.

Balin, R., & Jansen, K. (2021). Direct numerical simulation of a turbulent boundary layer over a bump with strong pressure gradients. *J. Fluid Mech.*, *918, A14*, 1–32.

Baskaran, V., Smits, A. J., & Joubert, P. N. (1987). A turbulent flow over a curved hill part 1. growth of an internal boundary layer. *J. Fluid Mech.*, *182*, 47–83.

Baskaran, V., Smits, A. J., & Joubert, P. N. (1991). A turbulent flow over a curved hill. part 2. effects of streamline curvature and streamwise pressure gradient. *J. Fluid Mech.*, *232*, 377–402.

Bonn, D., Amarouchene, Y., Wagner, C., Douady, S., & Cadot, O. (2005). Turbulent drag reduction by polymers. *J. Phys.: Condens. Matter*, *17*, S1195–S1202.

Ceccio, S. L., Perlin, M., & Elbing, B. R. (2010). A cost-benefit analysis for air layer drag reduction. *International Conference on Ship Drag Reduction*.

Ceccio, S. L., & Mäkiharju, S. A. (2012). Air lubrication drag reduction on great lakes ships.

Çengel, Y. A., & Cimbala, J. M. (2018). *Fluid mechanics : Fundamentals and applications* (Fourth). McGraw-Hill Education.

Chauhan, K. A., Monkewitz, P. A., & Nagib, H. M. (2009). Criteria for assessing experiments in zero pressure gradient boundary layers. *Fluid Dynamics Research*, *41*, 1–23.

Clauser, F. H. (1954). Turbulent boundary layers in adverse pressure gradients. *Journal of the Aeronautical Sciences*, *21 (2)*, 91–108.

Dean, B., & Bhushan, B. (2010). Shark-skin surfaces for fluid-drag reduction in turbulent flow: A review. *Philosophical Transactions of the Royal Society A: Mathematical, Physical and Engineering Sciences*, *368*, 4775–4806.

DeGraaff, D. B., & Eaton, J. K. (2000). Reynolds-number scaling of the flat-plate turbulent boundary layer. *Journal of Fluid Mechanics*, *422*, 319–346.

Elbing, B. R., Mäkiharju, S., Wiggins, A., Perlin, M., Dowling, D. R., & Ceccio, S. L. (2013). On the scaling of air layer drag reduction. *Journal of Fluid Mechanics*, *717*, 484–513.

Elbing, B. R., Winkel, E., A. Lay, K., Ceccio, S. L., Dowling, D. R., & Perlin, M. (2008). Bubble-induced skin-friction drag reduction and the abrupt transition to air-layer drag reduction. *Journal of Fluid Mechanics*, *612*, 201–236.

Elsinga, G. E., & Westerweel, J. (2012). Tomographic-piv measurement of the flow around a zigzag boundary layer trip. *Exp. Fluids*, *52*, 865–876.

Falco, R. E. (1977). Coherent motions in the outer region of turbulent boundary layers. *Phys. Fluids*, *20*, S124–S132.

Fukuda, K., Tokunaga, J., Nobunaga, T., Nakatani, T., Iwasaki, T., & Kunitake, Y. (2000). Frictional drag reduction with air lubricant over super-water repellent surface. *J Mar Sci Technology*, *5*, 123–130.

Harun, Z., Monty, J. P., Mathis, R., & Marusic, I. (2013). Pressure gradient effects on the large-scale structure of turbulent boundary layers. *J. Fluid Mech.*, *715*, 477–498.

Head, M. R., & Bandyopadhyay, P. R. (1981). New aspects of turbulent boundary-layer structure. *Journal of Fluid Mechanics*, *107*, 297–338.

Hutchins, N., Nickels, T. B., Marusic, I., & Chong, M. S. (2009). Hot-wire spatial resolution issues in wall-bounded turbulence. *Journal of Fluid Mechanics*, *635*, 103–136.

Jackson, P. S., & Hunt, J. C. R. (1975). Turbulent wind flow over a low hill. *Quart. J. R. Met. SOC.*, *101*, 929–955.

Kim, D., & Moin, P. (2010). Direct numerical study of air layer drag reduction phenomenon over backward-facing step. *Centre for Turbulence Research*, 351–363.

Kline, J., Reynolds, W. C., Schraub, R. A., & Runstadler, P. W. (1967). The structure of turbulent boundary layers. *Journal of Fluid Mechanics*, *30*, 741–773.

Latorre, R. (1997). Ship hull drag reduction using bottom air injection. *Ocean Engineering*, *2*, 161–175.

Mäkiharju, S. A., Perlin, M., & Ceccio, S. L. (2012). On the energy economics of air lubrication drag reduction. *International Journal of Naval Architecture and Ocean Engineering*, *4*, 412–422.

Mäkiharju, S. A., Lee, I.-H. R., Filip, G. P., Maki, K. J., & Ceccio, S. L. (2017). The topology of gas jets injected beneath a surface and subject to liquid cross-flow. *Journal of Fluid Mechanics*, *818*, 141–183.

Martinez de la Cruz, R. (2019). Msc thesis: Underwater drag reduction: Air layer stability over super-hydrophobic surface under turbulent conditions.

Monty, J., Harun, Z., & Marusic, I. (2011). A parametric study of adverse pressure gradient turbulent boundary layers. *International Journal of Heat and Fluid Flow*, *32*, 575–585.

Mukto, M. A., Atmane, M. A., & Loewen, M. R. (2007). A particle-image based wave profile measurement technique. *Exp Fluids*, *42*, 131–142.

Murai, Y. (2014). Frictional drag reduction by bubble injection. *Exp Fluids*, *55:1773*.

Nagano, Y., Tsuji, T., & Houra, T. (1998). Structure of turbulent boundary layer subjected to adverse pressure gradient. *International Journal of Heat and Fluid Flow*, *19*, 563–572.

Narasimha, R., & Sreenivasan, K. R. (1979). Relaminarization of fluid flows. *Advances in Applied Mechanics*, *19*, 222–303.

Nieuwstadt, F. T. M., Boersma, B. J., & Westerweel, J. (2016). *Turbulence: Introduction to theory and applications of turbulent flows*. Springer.

Nikolaidou, L., Laskari, A., Terwisga, T. v., & Poelma, C. (2021). On the characteristics of air layer regimes. *11th International Symposium on Cavitation*, 1–6.

Psaraftis, H. N., & Kontovas, C. A. (2020). Decarbonization of maritime transport: Is there light at the end of the tunnel? *Sustainability 2021*, *13*, 237–250.

Raffel, M., Willert, C. E., Scarano, F., Kähler, C. J., Wereley, S. T., & Kompenhans, J. (2018). *Particle image velocimetry: A practical guide* (Third). Springer International Publishing AG.

Robinson, S. K. (1991). Coherent motions in the turbulent boundary layer. *Annu. Rev. Fluid Mech*, *23*, 601–639.

Sanders, W. C., Winkel, E. S., Dowling, D. R., Perlin, M., & Ceccio, S. L. (2006). Bubble friction drag reduction in a high-reynolds-number flat-plate turbulent boundary layer. *Journal of Fluid Mechanics*, *552*, 353–380.

Saric, W. S. (1994). Görtler vortices. *Annual Rev: Fluid Mechanics*, *26*, 379–409.

Scarano, F. (2013). *Ae4180 course reader: Experimental aerodynamics* (First).

Schlichting, H., & Gersten, K. (2017). *Boundary-layer theory* (Ninth). Springer-Verlag.

Smits, A. J. (1985). The response of turbulent boundary layers to sudden perturbations. *Ann. Rev. Fluid Mech.*, *17*, 321–358.

So, R. M. C., & Mellor, G. L. (1973). Experiment on convex curvature effects in turbulent boundary layers. *J. Fluid Mech.*, *60*, 43–62.

So, R. M. C., & Mellor, G. L. (1975). Experiments on turbulent boundary layers on a concave wall. *The Aeronautical Quarterly*, *26*, 25–40.

Tardu, S. (1995). Characteristics of single and clusters of bursting events in the inner layer, part 1: Vita events. *Exp. Fluids*, *20*, 112–124.

Theodorsen, T. (1952). Mechanism of turbulence. *Proceedings of the Midwestern Conference on Fluid Mechanics*.

Tsikata, J., & Tachie, M. (2013). Effects of roughness and adverse pressure gradient on the turbulence structure. *International Journal of Heat and Fluid Flow*, *44*, 239–257.

Vinuesa, R., Bobke, R., A.and Örlü, & Schlatter, P. (2016). On determining characteristic length scales in pressure-gradient turbulent boundary layers. *Phys. Fluids*, *28*, 055101:1–13.

Webster, D. R., DeGraff, D. B., & Eaton, J. K. (1996). Turbulence characteristics of a boundary layer over a two-dimensional bump. *J. Fluid Mech.*, *320*, 53–69.

Westerweel, J., & Scarano, F. (2005). Universal outlier detection for piv data. *Experiments in Fluids*, *39*, 1096–1100.

Zverkhovskyi, O. (2014). Phd thesis: Ship drag reduction by air cavities.